Mechanical Systems and Signal Processing 150 (2021) 107301

Contents lists available at ScienceDirect

Mechanical Systems and Signal Processing

journal homepage: www.elsevier.com/locate/ymssp

A comb-like beam based piezoelectric system for galloping energy harvesting

Guobiao Hu [a,b], Junlei Wang [a,c,*], Lihua Tang [b,*]

[a] Engineering Research Center of Energy Saving Technology and Equipment of Thermal Energy System, Ministry of Education, Zhengzhou University, 100 Science Avenue, Zhengzhou 450000, China
[b] Department of Mechanical Engineering, The University of Auckland, 20 Symonds Street, Auckland 1010, New Zealand
[c] School of Mechanical and Power Engineering, Zhengzhou University, 100 Science Avenue, Zhengzhou 450000, China

ARTICLE INFO

Article history:
Received 30 May 2020
Received in revised form 25 July 2020
Accepted 9 September 2020

Keywords:
Metamaterial beam
Galloping
Energy harvesting
Multiple-degree-of-freedom
Piezoelectrics

ABSTRACT

This paper proposes a comb-like beam (CombBeam) based piezoelectric energy harvester (PEH) for harvesting wind energy by exploiting the galloping mechanism. The CombBeam-based PEH consists of a series of parasitic beams being mounted to a conventional cantilever beam with a piezoelectric transducer. A theoretical modelling method is established to simplify the proposed CombBeam-based PEH as a multiple-degree-of-freedom (MDOF) system. The conventional beam PEH is first represented as a single-degree-of-freedom (SDOF) system and the parasitic beam is then also converted into an equivalent SDOF system. A factor is derived to correct the reaction force of the SDOF model of the parasitic beam to address the force interaction between the host beam and the parasitic beam and a scaling factor is introduced to reflect the effect of the parasitic beam when being mounted onto the host beam at different positions. The complete mathematical formulations of the MDOF model for the CombBeam-based PEH under the base excitation and the aerodynamic force excitation are developed. Under the base excitation, a finite element model is built to first verify the MDOF model of the proposed CombBeam-based PEH in terms of derived equivalent lumped parameters, correction factors and scaling factor. A physical prototype of the proposed CombBeam PEH is then fabricated and the wind tunnel experiment is conducted to validate the MDOF model for predicting the energy harvesting performance under aerodynamic force excitation. The PEH undergoing galloping is referred as CombBeam-based GPEH to distinguish it with that under the base excitation. The results show that the CombBeam-based GPEH has the advantages over a conventional beam GPEH in reducing the cut-in wind speed from 2.24 m/s to 1.96 m/s and enhancing the power output around the optimal resistance for about 171.2% under a specific wind speed of 3 m/s.

---

[*] Corresponding authors at: Engineering Research Center of Energy Saving Technology and Equipment of Thermal Energy System, Ministry of Education, Zhengzhou University, 100 Science Avenue, Zhengzhou 450000, China (J. Wang); Department of Mechanical Engineering, The University of Auckland, 20 Symonds Street, Auckland 1010, New Zealand (L. Tang).

E-mail addresses: jlwang@zzu.edu.cn (J. Wang), l.tang@auckland.ac.nz (L. Tang).

https://doi.org/10.1016/j.ymssp.2020.107301

1. Introduction

In the past two decades, vibration energy harvesting has been extensively studied with the purpose to replace traditional chemical batteries for powering small electronic devices [1–9]. Vibration sources available for harvesting can be mainly classified into two categories: base vibration [10–12] and flow-induced vibration [13–18]. Mechanisms for generating flow-induced vibration include galloping [19–21], wake galloping [22,23], flutter [24] and vortex-induced vibration [25–28]. A recent review paper summarized the state-of-the-art of flow-induced vibration for energy harvesting [1]. To finally convert the vibration into desired electrical energy, electromagnetic [29], electrostatic [30], and piezoelectric [31,32] transduction methods can be employed. Because of the advantages of high power density and ease of implementation, using piezoelectric materials for energy harvesting has attracted numerous research interests.

Galloping-induced vibration has the characteristics of large oscillation amplitude and wide range of operating wind speed. Therefore, galloping piezoelectric energy harvesters (GPEHs) have been explosively researched. A conventional GPEH can be devised by attaching a bluff body to the tip of a piezoelectric beam [33]. In the wind flow, an aerodynamic fore acted onto the bluff body drives the piezoelectric beam to vibrate. The underlying physics is that the aerodynamic fore applied on the bluff body plays the role of negative damping that induces the aerodynamic instability. When this negative damping neutralizes the mechanical damping of the GPEH and the total damping of the system becomes negative, the instability is triggered and the GPEH eventually settles with limit cycle oscillations. Various models have been proposed to predict the performance of GPEHs. Since a cantilever beam can be modelled as a single-degree-of-freedom (SDOF) system [34,35], a GPEH that consists of a cantilever beam with a bluff body is often modelled as a SDOF system described by lumped parameters [17,27]. Besides the SDOF modelling method, Zhao et al. [36] developed an analytical model for a cantilever GPEH shunted to a synchronized charge extraction (SCE) interface circuit. Tang et al. [37] proposed an equivalent circuit model (ECM) which can bridge the mechanical and electrical domains to ease the analysis of GPEHs shunted to complicated interface circuits.

Improving the power output and reducing the cut-in wind speed for broadband operation are the two main concerns in the design of a GPEH. To this end, various innovative configurations have been proposed by researchers to improve the performance of GPEHs. Bibo et al. [19] proposed a bi-stable GPEH by introducing a magnetic nonlinearity. The result showed that once the inter-well oscillation of the bi-stable GPEH was activated, the enhanced power output of the GPEH could be achieved. Yang et al. [38] employed a double-beam system in the design of a novel galloping energy harvester and reduced the cut-in wind speed up to 41.9%. Wang et al. [39] added Y-shaped attachments on the bluff body of a wind energy harvester. The transition from vortex-induced vibrations into galloping was experimentally observed and the energy harvesting performance was enhanced. Instead of using a SDOF design of GPEH, Zhao et al. [40] built a nonlinear GPEH using a cut-out cantilever beam which was equivalent to a 2-DOF system. The experimental results showed that the cut-in wind speed was beneficially decreased and the power output was increased.

On the other hand, metamaterials with unique dynamic behaviours derived from artificially engineered micro-structures [41–43] have attracted increasing interests for being used in the design of novel vibration energy harvesting systems [44–50]. Shen et al. [51] designed a metamaterial plate using spiral beams as local resonators and readily available conversion medium for energy harvesting. The output power was enhanced at multiple resonant frequencies in the low frequency regime as compared to a similar plate without local resonators. Mikoshiba et al. [46] proposed a metamaterial with local resonators made of spring-suspended magnets to realize energy conversion. The experimental result showed that the proposed metamaterial based system could not only isolate vibrations but also convert vibrations into electricity. Liu et al. [52] designed a broadband acoustic energy harvester based on a *meta*-surface consisting of coupled Helmholtz resonators. An experimental evaluation showed that the proposed metamaterial based acoustic energy harvester could produce a high voltage output over a wide frequency range in 460–680 Hz. More recently, Chen et al. [53] proposed a metamaterial plate shunted to a self-powered synchronized charge extraction (SCE) circuit for energy harvesting. Based on the Kirchhoff plate theory and equivalent impedance method, they developed the theoretical model. The effects of the SCE circuit on the band gap behaviour of the metamaterial and the energy harvesting performance were investigated and validated by experiment.

According to the state-of-the art of the research, though metamaterials have been employed in designing vibration energy harvesters, the research is still limited to the base excitation generated vibration. Regarding flow-induced vibration energy harvesting, related research has not been found yet in the existing literature. In this paper, galloping energy harvesting is realized based on the structure composed of a metamaterial-inspired beam, a bluff body and a piezoelectric transducer. It is well known that an important feature of metamaterials is the structural periodicity. Since only a single piezoelectric transducer is bonded on the main beam rather than a series of periodic piezoelectric transducers embedded in the local resonators, we term the proposed design as a comb-like beam based galloping energy harvester according to the structural appearance. For conciseness, it is referred as “CombBeam-based GPEH” hereinafter. The rest of the paper is organized as follows: In Section 2, the design of the proposed CombBeam-based GPEH is briefly introduced. In Section 3, we present the theoretical modelling of the proposed CombBeam-based PEH. A MDOF model for describing the proposed CombBeam-based PEH is established. Mathematical formulations for describing the dynamic motion of the MDOF PEH under the base excitation and the aerodynamic force excitation are developed. Since both models under different excitations have similar mathematical formulations, except for the forcing load terms, the validation of the established MDOF model is proceeded from two aspects. In Section 4, the finite element method is used to verify the developed MDOF model for describing the proposed

CombBeam-based PEH under a base excitation. In Section 5, an experiment is conducted to evaluate the performance of the proposed CombBeam-based GPEH. The results are used to validate the developed MDOF model under aerodynamic force excitation. Section 6 summaries the findings from this work.

2. CombBeam-based GPEH

Fig. 1(a) shows the schematic of a conventional GPEH consisting of a cantilever beam attached with a square-sectioned bluff body and bonded with a piezoelectric transducer at the root. Fig. 1(b) shows the proposed CombBeam-based GPEH that is designed on the basis of a conventional GPEH. A series of parasitic beams are periodically mounted on the host beam by screw connection following the manner of a metamaterial beam. It is worth mentioning that a parasitic beam is actually split into two identical small cantilever beams by the host beam. This symmetric design is to minimize the torsional motion of the host beam due to any artificially introduced unexpected imbalance. The wind flows from the right to left and the wind direction is in parallel to the beam length direction. The aerodynamic force acted on the bluff body causes the beam to vibrate in the beam thickness direction. The bonded piezoelectric transducer converts the galloping-induced vibrations into electrical energy.

3. Theoretical modelling

3.1. Equivalent lumped parameters of parasitic beam

A parasitic beam is treated as two identical cantilevered beams which can be represented as a single SDOF system with lumped parameters. Fig. 2 shows the diagram of the parasitic beam with annotations of dimensional parameters. The equivalent mass m_a, stiffness k_a and damping coefficient c_a can be derived as:

$$\begin{cases} m_a = \frac{1}{\phi_{1a}^2(L_a)} & k_a = \frac{\omega_{1a}^2}{\phi_{1a}^2(L_a)} \\ c_a = \frac{2\zeta_{1a}\omega_{1a}}{\phi_{1a}^2(L_a)} & \mu_a = \phi_{1a}(L_a)\gamma_{1a} \end{cases} \tag{1}$$

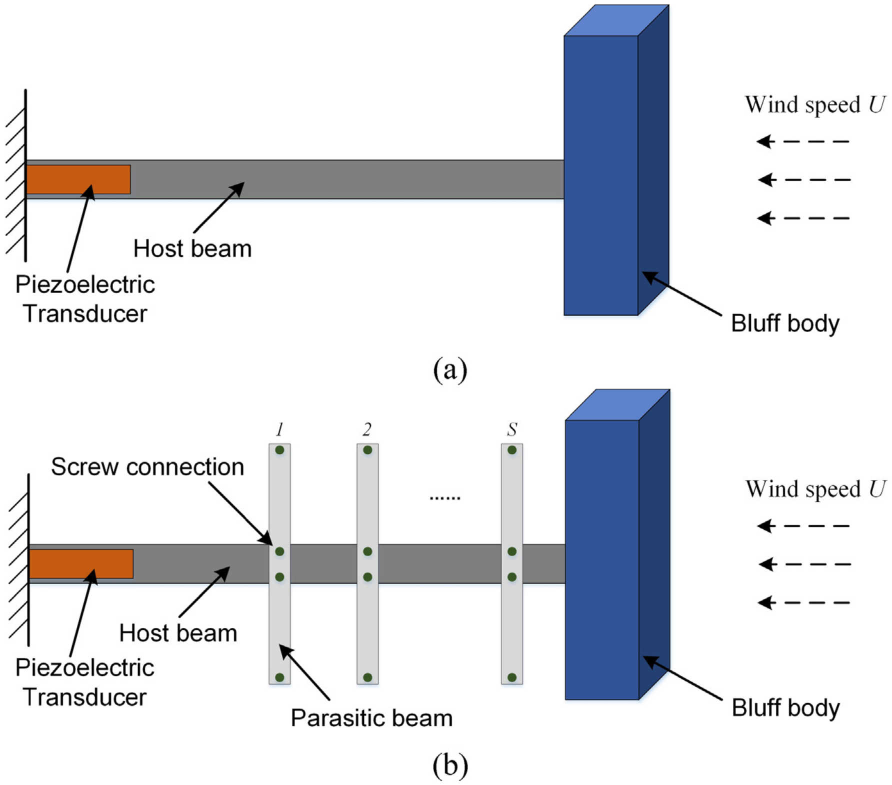

Fig. 1. Schematic of (a) conventional GPEH and (b) CombBeam-based GPEH.

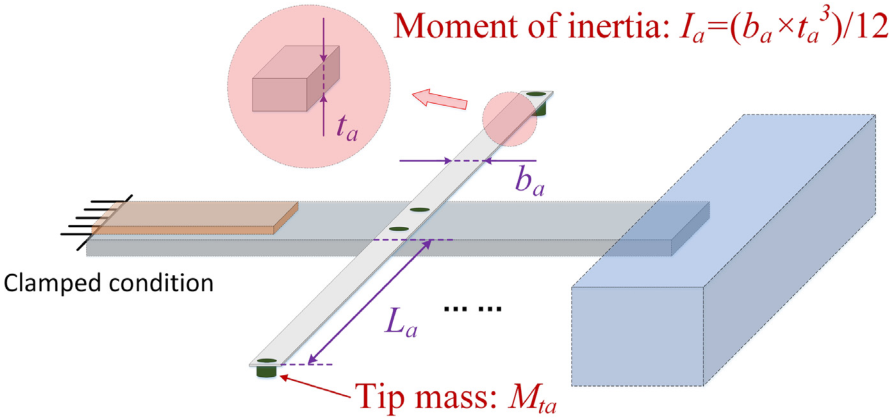

Fig. 2. Diagram of the parasitic beam with annotations of dimensional parameters.

where L_a is the length of the parasitic beam. ζ_{1a} is the damping ratio. $\gamma_{1a} = \int_{x=0}^{L_a} m\phi_{1a}(x)dx + \phi_{1a}(L_a)M_{ta}$ in which m denotes the mass per unit length of the parasitic beam and M_{ta} represents the tip mass attached at the tip of the parasitic beam. $\phi_{1a}(x)$ is the mass normalized fundamental mode shape of the parasitic beam. μ_a is a factor applied to the forcing term to convert the distributed load applied on the beam into an equivalent concentrated force. ω_{1a} is the fundamental natural frequency of the parasitic beam that can be determined from the following characteristic equation:

$$\left[1+\cos(\beta_{1a}L_a)\cosh(\beta_{1a}L_a)+\frac{\beta_{1a}M_{ta}}{m}(\cos(\beta_{1a}L_a)\sin(\beta_{1a}L_a)-\sin(\beta_{1a}L_a)\cosh(\beta_{1a}L_a))\right]=0 \tag{2}$$

where $\beta_{1a}^4 = \omega^2 m/E_aI_a$. After determining β_{1a} from Eq. (2), the explicit expression of $\phi_{1a}(x)$ can be written as:

$$\phi_{1a}(x) = C_1[\cos(\beta_a x) - \cosh(\beta_a x) + \sigma_{1a}(\sin(\beta_a x) - \sinh(\beta_a x))] \tag{3}$$

where $\sigma_{1a} = \frac{m(\sin(\beta_{1a}L_a)-\sinh(\beta_{1a}L_a))+\beta_{1a}M_{ta}(\cos(\beta_{1a}L_a)-\cosh(\beta_{1a}L_a))}{m(\cos(\beta_{1a}L_a)+\cosh(\beta_{1a}L_a))-\beta_{1a}M_{ta}(\sin(\beta_{1a}L_a)-\sinh(\beta_{1a}L_a))}$. C_1 is a constant that is determined in the mass normalization process to satisfy the following orthogonality relation:

$$\int_{x=0}^{L_a}\phi_{1a}(x)m\phi_{1a}(x)dx + \phi_{1a}(L_a)M_{ta}\phi_{1a}(L_a) = 1 \tag{4}$$

The parasitic beam has already been represented by a SDOF model by assuming that the lumped parameters are concentrated at the beam tip. However, the derived lumped parameters are only effective parameters at the beam tip. The reaction force of the parasitic beam at the root can be analytically expressed as:

$$f^R(t) = E_aI_a\frac{\partial^3 w_a(x,t)}{\partial x^3}\bigg|_{x=0} + c_{sa}I_a\frac{\partial^4 w_a(x,t)}{\partial x^3\partial t}\bigg|_{x=0} \tag{5}$$

where the first term and the second term denote the stiffness and damping-related forces, respectively. $w_a(x,t)$ is the deflection of the parasitic beam relative to the base. It is worth mentioning that when the parasitic beam is later attached to the host beam, the "base" here will refer to the "host beam". $\eta_{1a}(t)$ is the modal coordinate of the fundamental mode. c_{sa} is the equivalent coefficient of strain rate damping that can be expressed using the damping ratio ζ_{1a} as $c_{sa} = 2E_a/\omega_{1a}\zeta_{1a}$. Using mode-superposition method and only keeping the first mode, we have $w_a(x,t) = \phi_{1a}(x)\eta_{1a}(t)$. Substituting $w_a(x,t) = \phi_{1a}(x)\eta_{1a}(t)$ into Eq. (5) and assuming $\eta_{1a}(t)$ to be time harmonic yields:

$$\begin{aligned} f^R(t) = & \ (1+2j\omega\zeta_{1a}\omega_{1a})\eta_{1a}(t)\left[-\int_{x=0}^{L_a}E_aI_a\frac{d^4\phi_{1a}(x)}{dx^4}dx + E_aI_a\frac{\partial^3\phi_{1a}(x)}{\partial x^3}\bigg|_{x=L_a}\right] \\ = & \ -(1+2j\omega\zeta_{1a}\omega_{1a})\eta_{1a}(t)\left[\int_{x=0}^{L_a}E_aI_a\frac{d^4\phi_{1a}(x)}{dx^4}dx + \omega^2 M_{ta}\right] \end{aligned} \tag{6}$$

On the other hand, the reaction force of the SDOF model of the parasitic beam can be calculated as:

$$\begin{aligned} -[k_a u_a(t) + c_a\dot{u}_a(t)] &= -(1+2j\omega\zeta_{1a}\omega_{1a})\frac{\omega_{1a}^2}{\phi_{1a}^2(L_a)}[\phi_{1a}(L_a)\eta_{1a}(t)] \\ &= -(1+2j\omega\zeta_{1a}\omega_{1a})\frac{\eta_{1a}(t)}{\phi_{1a}(L)}\left[\int_{x=0}^{L_a}E_aI_a\frac{d^4\phi_{1a}(x)}{dx^4}\phi_{1a}(x)dx\right] \end{aligned} \tag{7}$$

where $u_a(t)$ is the displacement of the parasitic beam tip relative to the base. Again, the "base" here will refer to the "host beam" if the parasitic beam is attached to the host beam. $-k_a u_a(t)$ and $-c_a \dot{u}_a(t)$ are the stiffness and damping-related forces, respectively. The relationship between the actual reaction force of the resonant beam and the reaction force calculated using the simplified SDOF model is:

$$\alpha = \frac{f^R(t)}{-[k_a u_a(t) + c_a \dot{u}_a(t)]} = \begin{bmatrix} \frac{m\phi_{1a}(L)\int_{x=0}^{L_a}\phi_{1a}(x)dx + \phi_{1a}^2(L)M_{ta}}{m\int_{x=0}^{L_a}\phi_{1a}^2(x)dx} \\ +\phi_{1a}(L)\frac{\omega^2}{\omega_{1a}^2}M_{ta} - \frac{\phi_{1a}^2(L)M_{ta}}{m\int_{x=0}^{L_a}\phi_{1a}^2(x)dx} \end{bmatrix} \tag{8}$$

Neglecting the small terms in Eq. (8), one can use μ_a as the approximated α to correct the reaction force of the parasitic beam calculated using the simplified SDOF model. It is worth mentioning that since a parasitic beam is split into two identical cantilever beams as explained in Section 1, when converting the parasitic beam into an equivalent SDOF model, it needs to be first processed with one cantilever beam to obtain its equivalent lumped parameters, and then the equivalent lumped parameters (i.e., m_a, k_a and c_a) of the parasitic beam should double those of a single cantilever. However, the correction factors, i.e., μ_a and α, remain the same.

3.2. Equivalent lumped parameters of host beam

Since the parasitic beam has already been represented by a SDOF system with the correction of the reaction force at the root, the governing equations of the whole structure can be expressed as:

$$\begin{cases} EI_1\frac{\partial^4 w_1(x_1,t)}{\partial x_1^4} + c_s I_1 \frac{\partial^3 w_1(x_1,t)}{\partial x_1^2 \partial t} + m_1 \frac{\partial^2 w_1(x_1,t)}{\partial t^2} + \vartheta v(t) \times \left[\frac{d\delta(x_1)}{dx_1} - \frac{d\delta(x_1 - L_1)}{dx_1}\right] = -m_1 \ddot{w}_b(t) \\ EI_2\frac{\partial^4 w_2(x_2,t)}{\partial x_2^4} + c_s I_2 \frac{\partial^3 w_2(x_2,t)}{\partial x_2^2 \partial t} + m_2 \frac{\partial^2 w_2(x_2,t)}{\partial t^2} = \left\{ \begin{array}{c} -[m_2 + M_t\delta(x_2 - L_2)]\ddot{w}_b(t) \\ +M_t d_c \frac{d\delta(x_2 - L_2)}{dx}\ddot{w}_b(t) \\ -\sum_{i=1}^{S} F_i^R \delta\left(x - x_i^R\right) e^{j\omega t} \end{array} \right\} \\ m_a \ddot{u}_{1,rel}^R(t) + c_a \dot{u}_{1,rel}^R(t) + k_a u_{1,rel}^R(t) = -m_a\left[\ddot{w}_2\left(x_1^R, t\right) + \ddot{w}_b(t)\right] \\ \vdots \\ m_a \ddot{u}_{S,rel}^R(t) + c_a \dot{u}_{S,rel}^R(t) + k_a u_{S,rel}^R(t) = -m_a\left[\ddot{w}_2\left(x_S^R, t\right) + \ddot{w}_b(t)\right] \end{cases} \tag{9}$$

where $j = \sqrt{-1}$ is the imaginary unit, x_1 and x_2 are the local spatial coordinates of the beam sections with and without piezoelectric coverage ($0 \leqslant x_1 \leqslant L_1$ and $0 \leqslant x_2 \leqslant L_2$).$w_1(x_1, t)$ and $w_2(x_2, t)$ represent the beam deflections relative to the base motion $w_b(t)$. $\delta(x)$ is the Dirac delta function. $\vartheta = -e_{31} b_p h_{pc}$ is the piezoelectric coupling term, in which h_{pc} is the position of the centre of the piezoelectric layer to the neutral axis and $e_{31} = E_p d_{31}$ is the piezoelectric constant in the unit of C/m^2. d_{31} is the piezoelectric constant in the unit of C/N. M_t is the tip mass (bluff body). d_c is the distance from the centre of gravity of the bluff body to its attaching point on the host beam. F_i^R is the reaction force applied on the host beam by the i-th parasitic beam (local resonator). m_1 and m_2 are the mass per unit length and EI_1 and EI_2 are the bending stiffnesses of the two beam sections, respectively. These parameters can be calculated by using the geometric and material properties of the beam as:

$$\begin{cases} m_1 = \rho_s h_s b_s + \rho_p h_p b_p \\ m_2 = \rho_s h_s b_s \\ EI_1 = E_s b_s \left(h_b^3 - h_a^3\right)/3 + E_p b_p \left(h_c^3 - h_b^3\right)/3 \\ EI_2 = E_s b_s h_s^3/12 \end{cases} \tag{10}$$

where E_s and E_p are the Young's moduli of the substrate and piezoelectric layers, respectively. h_a is the position of the bottom surface of the substrate layer to the neutral axis, h_b and h_c are the positions of the bottom and top of the piezoelectric layer to the neutral axis, respectively. These parameters including the aforementioned h_{pc} are dependent on the material and geometric properties of the substrate and piezoelectric layers. They can be calculated using the following expressions.

$$\begin{cases} h_a = -\frac{E_p b_p h_p \left(2h_s + h_p\right) + E_s b_s h_s^2}{2\left(E_p b_p h_p + E_s b_s h_s\right)} \\ h_b = h_s + h_a \\ h_c = h_p + h_b \\ h_{pc} = \frac{h_b + h_c}{2} \end{cases} \tag{11}$$

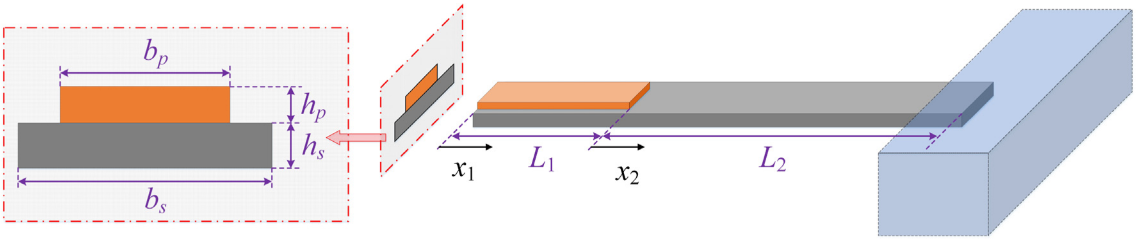

Fig. 3. Diagram of the host beam with annotations of dimensional parameters.

To simplify the host beam as a SDOF system as well, we first consider the host beam only which is shown in Fig. 3. Neglecting the parasitic beams yields a conventional beam PEH for which the governing equations of the beam regarding the sections with and without the piezoelectric layer are written as:

$$\begin{cases} EI_1\frac{\partial^4 w_1(x_1,t)}{\partial x_1^4}+m_1\frac{\partial^2 w_1(x_1,t)}{\partial t^2}+\vartheta v(t)\times\left[\frac{d\delta(x_1)}{dx_1}-\frac{d\delta(x_1-L_1)}{dx_1}\right]=-m_1\ddot{w}_b(t) \\ EI_2\frac{\partial^4 w_2(x_2,t)}{\partial x_2^4}+m_2\frac{\partial^2 w_2(x_2,t)}{\partial t^2}=-\left[m_2+M_t\delta(x_2-L_2)-M_t d_c\frac{d\delta(x_2-L_2)}{dx}\right]\ddot{w}_b(t) \end{cases} \tag{12}$$

First, to determine the natural frequencies and mode shapes of the beam, the electromechanical coupling term, the damping term and the forcing term are temporarily dropped. Using the variable-separation approach, we can assume the solution of the beam deflection by variable separation in the form as:

$$w_k(x_k,t)=\phi_k(x_k)\eta(t) \tag{13}$$

where the subscript k = 1,2 denotes two beam sections. $\phi_k(x_k)$ is the shape function and $\eta(t)$ is the time dependent quantity and is assumed to be time harmonic. Substituting Eq. (13) into Eq. (12) and neglecting $\eta(t)$ that applies to all the field variables, the governing equation for the free vibration of the beam is then simplified as:

$$EI_k\frac{d^4\phi_k(x_k)}{dx^4}-\omega^2 m_k\phi_k(x_k)=0 \tag{14}$$

The solutions to Eq. (14) are assumed in the form as follows:

$$\begin{cases} \phi_1(x_1)=\begin{bmatrix} A_1\sin\beta_1x_1+B_1\cos\beta_1x_1 \\ +C_1\sinh\beta_1x_1+D_1\cosh\beta_1x_1 \end{bmatrix} \\ \phi_2(x_2)=\begin{bmatrix} A_2\sin\beta_2x_2+B_2\cos\beta_2x_2 \\ +C_2\sinh\beta_2x_2+D_2\cosh\beta_2x_2 \end{bmatrix} \end{cases} \tag{15}$$

in which $\beta_k^4=\omega^2 m_k/EI_k$. The boundary conditions (i.e., clamped end, free end and continuities) are mathematically expressed as follows:

$$\begin{cases} \phi_1(0)=0 \\ \phi_1'(0)=0 \\ \phi_1(L_1)=\phi_2(0) \\ \phi_1'(L_1)=\phi_2'(0) \\ EI_1\phi_1''(L_1)=EI_2\phi_2''(0) \\ EI_1\phi_1'''(L_1)=EI_2\phi_2'''(0) \\ EI_2\phi_2''(L_2)=J_t\omega^2\phi_2'(L_2)+M_t d_c\omega^2\phi_2(L_2) \\ EI_2\phi_2'''(L_2)=-M_t d_c\omega^2\phi_2'(L_2)-M_t\omega^2\phi_2(L_2) \end{cases} \tag{16}$$

where J_t is the moment of inertia of the tip mass about the axis that passes through the attaching point. By substituting Eq. (15) into Eq. (16) and re-expressing in the matrix form, then letting the determinant of the coefficient matrix to be of zero in order to have a non-trivial solution, one obtains:

$$\begin{vmatrix} \begin{pmatrix} T_1N_1+T_2N_3 \\ +T_3N_5+T_4N_7 \end{pmatrix} & \begin{pmatrix} T_1N_2+T_2N_4 \\ +T_3N_6+T_4N_8 \end{pmatrix} \\ \begin{pmatrix} T_5N_1+T_6N_3 \\ +T_7N_5+T_8N_7 \end{pmatrix} & \begin{pmatrix} T_5N_2+T_6N_4 \\ +T_7N_6+T_8N_8 \end{pmatrix} \end{vmatrix}=0 \tag{17}$$

where

$$\begin{cases} N_1 = [(R_1 + R_3)\cos\beta_1 L_1 - (R_1 - R_3)\cosh\beta_1 L_1]/2 \\ N_2 = -[(R_3 + R_1)\sin\beta_1 L_1 + (R_1 - R_3)\sinh\beta_1 L_1]/2 \\ N_3 = [(1 + R_2)\sin\beta_1 L_1 - (1 - R_2)\sinh\beta_1 L_1]/2 \\ N_4 = [(1 + R_2)\cos\beta_1 L_1 - (1 - R_2)\cosh\beta_1 L_1]/2 \\ N_5 = [(R_1 - R_3)\cos\beta_1 L_1 - (R_1 + R_3)\cosh\beta_1 L_1]/2 \\ N_6 = [(R_3 - R_1)\sin\beta_1 L_1 - (R_3 + R_1)\sinh\beta_1 L_1]/2 \\ N_7 = [(1 - R_2)\sin\beta_1 L_1 - (1 + R_2)\sinh\beta_1 L_1]/2 \\ N_8 = [(1 - R_2)\cos\beta_1 L_1 - (1 + R_2)\cosh\beta_1 L_1]/2 \end{cases} \quad \begin{cases} R_1 = \frac{\beta_1}{\beta_2} \\ R_2 = \frac{E_1 I_1 \beta_1^2}{E_2 I_2 \beta_2^2} \\ R_3 = \frac{E_1 I_1 \beta_1^3}{E_2 I_2 \beta_2^3} \end{cases}$$

$$\begin{cases} T_1 = \left[-\left(EI_2\beta_2^2 + M_t d_c \omega^2\right)\sin(\beta_2 L_2) - J_t \omega^2 \beta_2 \cos(\beta_2 L_2)\right] \\ T_2 = \left[-\left(EI_2\beta_2^2 + M_t d_c \omega^2\right)\cos(\beta_2 L_2) + J_t \omega^2 \beta_2 \sin(\beta_2 L_2)\right] \\ T_3 = \left[\left(EI_2\beta_2^2 - M_t d_c \omega^2\right)\sinh(\beta_2 L_2) - J_t \omega^2 \beta_2 \cosh(\beta_2 L_2)\right] \\ T_4 = \left[\left(EI_2\beta_2^2 - M_t d_c \omega^2\right)\cosh(\beta_2 L_2) - J_t \omega^2 \beta_2 \sinh(\beta_2 L_2)\right] \\ T_5 = \left[\left(-EI_2\beta_2^3 + M_t d_c \omega^2 \beta_2\right)\cos(\beta_2 L_2) + M_t \omega^2 \sin(\beta_2 L_2)\right] \\ T_6 = \left[\left(EI_2\beta_2^3 - M_t d_c \omega^2 \beta_2\right)\sin(\beta_2 L_2) + M_t \omega^2 \cos(\beta_2 L_2)\right] \\ T_7 = \left[\left(EI_2\beta_2^3 + M_t d_c \omega^2 \beta_2\right)\cosh(\beta_2 L_2) + M_t \omega^2 \sinh(\beta_2 L_2)\right] \\ T_8 = \left[\left(EI_2\beta_2^3 + M_t d_c \omega^2 \beta_2\right)\sinh(\beta_2 L_2) + M_t \omega^2 \cosh(\beta_2 L_2)\right] \end{cases}$$

Solving Eq. (17) yields the natural frequencies and the mode shapes of this conventional beam PEH. Moreover, using the boundary conditions presented in Eq. (16), the orthogonality relations can be derived as follows:

$$\begin{cases} \begin{bmatrix} \int_{x=0}^{L_1} m_1 \phi_{1,j}(x)\phi_{1,i}(x)dx + \int_{x=0}^{L_2} m_2 \phi_{2,j}(x)\phi_{2,i}(x)dx + M_t \phi_{2,i}(L_2)\phi_{2,j}(L_2) \\ +M_t d_c \phi_{2,i}(L_2)\phi'_{2,j}(L_2) + M_t d_c \phi'_{2,i}(L_2)\phi_{2,j}(L_2) + J_t \phi'_{2,i}(L_2)\phi'_{2,j}(L_2) \end{bmatrix} = \delta_{ij} \\ \begin{bmatrix} \int_{x=0}^{L_1} EI_1 \frac{d^4\phi_{1,i}(x)}{dx^4} \frac{d\phi_{1,j}(x)}{dx} dx + \int_{x=0}^{L_2} EI_2 \frac{d^4\phi_{2,i}(x)}{dx^4} \frac{d\phi_{2,j}(x)}{dx} dx \\ -\left[\phi_{2,j}(x) EI_2 \frac{d^3\phi_{2,i}(x)}{dx^3}\right]_{x=L_2} + \left[\frac{d\phi_{2,j}(x)}{dx} EI_2 \frac{d^2\phi_{2,i}(x)}{dx^2}\right]_{x=L_2} \end{bmatrix} = \omega_i^2 \delta_{ij} \end{cases} \tag{18}$$

where $\phi_{k,i}(x_k)$ is the i-th mode shape. For the forced vibration of the conventional beam PEH, using the modal superposition method, the relative displacement of the beam sections $w_k(x_k, t)$ can be expressed as the summation of the product of mode shapes and modal coordinates as:

$$w_k(x_k, t) = \sum_{r=1}^{\infty} \phi_{k,r}(x_k)\eta_r(t) \tag{19}$$

where $\eta_r(t)$ is the modal coordinate of the r-th mode. Substituting Eq. (19) into Eq. (12), then using the orthogonality relations given in Eq. (18), the modal mechanical governing equation can be obtained:

$$\frac{d^2\eta_r(t)}{dt^2} + 2\zeta_r\omega_r \frac{d\eta_r(t)}{dt} + \omega_r^2 \eta_r(t) + \chi_r v(t) = \gamma_r A_{cc} e^{j\omega t} \tag{20}$$

$$\text{where } \chi_r = \vartheta \frac{d\phi_{1,r}(x_1)}{dx_1}\bigg|_{x_1=L_1}, \quad \gamma_r = -\begin{Bmatrix} \int_{x_1=0}^{L_1} \phi_{1,r}(x_1) m_1 dx_1 + \int_{x_2=0}^{L_2} \phi_{2,r}(x_2)[m_2 + M_t\delta(x_2 - L_2)]dx_2 \\ - \int_{x_2=0}^{L_2} \phi_{2,r}(x_2) M_t d_c \frac{d\delta(x_2 - L_2)}{dx} dx_2 \end{Bmatrix}$$

ω_r is the natural frequency of the r-th mode and A_{cc} is the amplitude of the acceleration of the base $\ddot{w}_b(t)$, i.e., $\ddot{w}_b(t) = -A_{cc}e^{j\omega t}$. The steady-state voltage response has the form of $v(t) = V_p e^{j\omega t}$. The modal response can then be obtained as:

$$\eta_r(t) = \frac{(\gamma_r A_{cc} - \chi_r V_p)e^{j\omega t}}{\omega_r^2 - \omega^2 + j2\zeta_r\omega_r\omega} \tag{21}$$

The relative displacement at the free end can thus be expressed by substituting Eq. (21) into Eq. (13):

$$w_2(L_2, t) = \sum_{r=1}^{\infty} \frac{\phi_{2,r}(L_2)(\gamma_r A_{cc} - \chi_r V_p)e^{j\omega t}}{\omega_r^2 - \omega^2 + j2\zeta_r\omega_r\omega} \tag{22}$$

The linear-electroelastic constitutive relation for the piezoelectric material is expressed as:

$$D_e(x_1, t) = e_{31}S(x_1, t) + \varepsilon_{33}^S E_3(t) \tag{23}$$

where $S(x_1,t)$ is the bending strain, $D_e(x_1,t)$ is the electric displacement, ε_{33}^S is the permittivity at constant stress of the piezoelectric transducer. The electric field in the piezoelectric transducer in terms of the voltage across it can be expressed as $E_3(t) = -v(t)/h_p$. According to the Euler- Bernoulli beam theory, the average bending strain in the piezoelectric transducer can be expressed as$S(x_1,t) = -h_{pc}\left[\partial^2 w_1(x_1,t)/\partial x_1^2\right]$. Therefore, Eq. (23) becomes:

$$D_e(x_1,t) = -e_{31} h_{pc} \frac{\partial^2 w_1(x_1,t)}{\partial x_1^2} - \varepsilon_{33}^S \frac{v(t)}{h_p} \tag{24}$$

Integrating the electric displacement over the electrode area and then differentiating with respect to time provides the current $i_p(t)$ flowing out of the piezoelectric transducer as follows:

$$i_p(t) = \vartheta \int_{x_1=0}^{L_1} \frac{\partial^3 w_1(x_1,t)}{\partial x_1^2 \partial t} dx - C_p \frac{dv(t)}{dt} \tag{25}$$

where $C_p = \varepsilon_{33}^S b L_1 / h_p$ represents the capacitance of the piezoelectric transducer. The clamped boundary condition implies that $\frac{\partial^2 w_1(0,t)}{\partial x_1 \partial t} = 0$ at x_1 = 0. Eq. (25) thus becomes:

$$i_p(t) = \vartheta \frac{\partial^2 w_1(x_1,t)}{\partial x_1 \partial t}\bigg|_{x_1=L_1} - C_p \frac{dv(t)}{dt} \tag{26}$$

The governing equations of the electromechanical system are formed by Eq. (20) and Eq. (26). In the following, the mode shapes of this system are determined. Then, based on the calculated mode shapes, the modal superposition method is employed to derive the closed-form solution of the electromechanically coupled equations. Substituting Eq. (19) into Eq. (26) yields the modal circuit governing equation:

$$C_p \frac{dv(t)}{dt} + i_p(t) = \sum_{r=1}^{\infty} \chi_r \frac{d\eta_r(t)}{dt} \tag{27}$$

Considering that the cantilever beam PEH is shunted to a resistor R_{load}, i.e., $i_p(t) = v(t)/R_{load}$, then combining Eq. (27) and Eq. (21), one can solve for V_p as:

$$V_p = \frac{\sum_{r=1}^{\infty} \chi_r \frac{j\omega\gamma_r A_{cc}}{\omega_r^2 - \omega^2 + j2\zeta_r\omega_r\omega}}{\left\{\left(\frac{1}{R_{load}} + j\omega C_p\right) + \sum_{r=1}^{\infty} \frac{j\omega\chi_r^2}{\omega_r^2 - \omega^2 + j2\zeta_r\omega_r\omega}\right\}} \tag{28}$$

Eq. (28) provides the analytical solution to the voltage response of the cantilever beam PEH. However, its formulation is relatively cumbersome. According to the literature, using the fundamental mode is sufficiently accurate to predict the energy harvesting performance around the fundamental resonance. Hence, by considering the fundamental mode and taking the tip displacement as degree of freedom, the cantilever beam PEH can be equivalently represented as a SDOF system (as shown in Fig. 4) with the lumped parameters [54]

$$\begin{cases} M = \frac{1}{\phi_{2,1}^2(L_2)} \quad K = \frac{\omega_1^2}{\phi_{2,1}^2(L_2)} \quad D = \frac{2\zeta_1\omega_1}{\phi_{2,1}^2(L_2)} \\ \Theta = \frac{\chi_1}{\phi_{2,1}(L_2)} \quad \mu = \phi_{2,1}(L_2)\gamma_1 \quad u_h(t) = \phi_{2,1}(L_2)\eta_1(t) \end{cases} \tag{29}$$

and the governing equations of the SDOF model can be obtained by rearranging Eqs. (20) and (27) as:

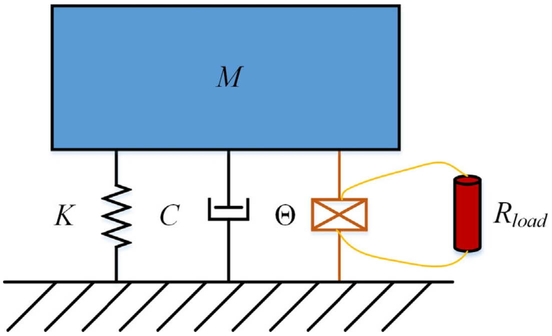

Fig. 4. Equivalent SDOF model of a cantilever beam PEH under base excitation.

$$\begin{cases} M\ddot{u}_h(t) + D\dot{u}_h(t) + Ku_h(t) + \Theta v(t) = -\mu M A_{cc} e^{j\omega t} \\ \frac{v(t)}{R_{load}} + C_p \dot{v}(t) = \Theta \dot{u}_h(t) \end{cases} \tag{30}$$

It is worth noting that the tip displacement of the host beam relative to the base is redefined as $u_h(t)$ for conciseness.

3.3. Position-dependent scaling factor of parasitic beam

Following the same procedure for obtaining Eq. (20), applying the same manipulation to Eq. (9), the modal governing equation of the host beam mounted with parasitic beams can be obtained:

$$\ddot{\eta}_1(t) + 2\zeta_1\omega_1\dot{\eta}_1(t) + \omega_1^2\eta_1(t) + \chi_1 v(t) = -\gamma_1 A_{cc} e^{j\omega t} - \sum_{i=1}^{S} F_i^R \phi_{2,1}\left(x_i^R\right) e^{j\omega t} \tag{31}$$

Dividing both sides of Eq. (31) by $\phi_{2,1}(L_2)$ and noting that the equivalent lumped parameters of the host beam with the tip mass given in Eq. (29). Rearranging the resultant equation (i.e., dividing both sides of Eq. (31) by $\phi_{2,1}(L_2)$) yields:

$$M\ddot{u}_h(t) + D\dot{u}_h(t) + Ku_h(t) + \Theta v(t) = -\mu M A_{cc} e^{j\omega t} - \sum_{i=1}^{S} \underbrace{\frac{\phi_{2,1}\left(x_i^R\right)}{\phi_{2,1}(L_2)}}_{\kappa_i} F_i^R e^{j\omega t} \tag{32}$$

where κ_i is the scaling factor that reflects the effect of the i-th parasitic beam on the host beam when being mounted at the position of x_i^R. Considering that the excitation of the i-th parasitic beam can be expressed in terms of the tip displacement of the host beam relative to the base (i.e., $u_h(t)$):

$$w\left(x_i^R, t\right) = \frac{\phi_{2,1}\left(x_i^R\right)}{\phi_{2,1}(L_2)} w(L_2, t) = \frac{\phi_{2,1}\left(x_i^R\right)}{\phi_{2,1}(L_2)} u_h(t) = \kappa_i u_h(t) \tag{33}$$

and the parasitic beam has already been represented by a SDOF system in Section 3.1, the governing equations of the i-th parasitic beam (i.e., local resonator) can be rewritten as:

$$m_a\ddot{u}_i(t) + c_a[\dot{u}_i(t) - \kappa_i\dot{u}_h(t)] + k_a[u_i(t) - \kappa_i u_h(t)] = -\mu_a m_a \ddot{u}_b(t) \tag{34}$$

where $u_i(t)$ is the tip displacement of the i-th parasitic beam relative to the base. It should be noted that $w\left(x_i^R, t\right) = \kappa_i u_h(t)$ is the displacement of the attaching point on the host beam of the i-th parasitic beam relative to the base. The reaction force of the i-th parasitic beam should be defined in terms of the displacement relative to the attaching point on the host beam, i.e. $u_i(t) - \kappa_i u_h(t)$, as

$$F_i^R e^{j\omega t} = f_i^R(t) = -\alpha\{c_a[\dot{u}_i(t) - \kappa_i\dot{u}_h(t)] + k_a[u_i(t) - \kappa_i u_h(t)]\} \tag{35}$$

It is worth mentioning that α is the reaction force factor that has already been derived in Section 3.1. Also, the "base" in Section 3.1 is the attaching point on the host beam here and therefore $u_a(t)$ in Eq. (8) should be replaced by $u_i(t) - \kappa_i u_h(t)$ here. Substituting Eq. (35) into Eq. (32), the governing equations of the host beam can be obtained as:

$$M\ddot{u}_h(t) + D\dot{u}_h(t) + Ku_h(t) + \Theta v(t) + \sum_{i=1}^{S} \alpha\left\{\kappa_i^2 c_a\left[\dot{u}_h(t) - \frac{\dot{u}_i(t)}{\kappa_i}\right] + \kappa_i^2 k_a\left[u_h(t) - \frac{u_i(t)}{\kappa_i}\right]\right\} = -\mu M A_{cc} e^{j\omega t} \tag{36}$$

3.4. MDOF model under base excitation

Both the host beam and the parasitic beams have been individually converted into equivalent independent SDOF systems. Using the derived scaling factor in Section 3.3 to address the coupling between the host beam and the parasitic beams, an equivalent MDOF model as shown in Fig. 5 for the proposed CombBeam-based PEH can be constructed. Letting $\underset{\sim}{u}_{i} = u_i(t)/\kappa_i$, $\underset{\sim}{m}_{a,i} = \kappa_i^2 m_a$, $\underset{\sim}{c}_{a,i} = \kappa_i^2 c_a$, $\underset{\sim}{k}_{a,i} = \kappa_i^2 k_a$ and $\underset{\sim}{A}_{cc} = A_{cc}/\kappa_i$, the governing equations of the MDOF model for the CombBeam-based PEH under translational base excitation can be formulated in the form as:

$$\begin{cases} \left\{M\ddot{u}_h(t) + D\dot{u}_h(t) + Ku_h(t) + \Theta v(t) + \sum_{i=1}^{S}\alpha\left[\underset{\sim}{c}_{a,i}\left(\dot{u}_h(t) - \underset{\sim}{\dot{u}}_{i}(t)\right) + \underset{\sim}{k}_{a,i}\left(u_h(t) - \underset{\sim}{u}_{i}(t)\right)\right]\right\} = -\mu M A_{cc} e^{j\omega t} \\ \underset{\sim}{m}_{a,i}\underset{\sim}{\ddot{u}}_{i} + \underset{\sim}{c}_{a,i}\left(\underset{\sim}{\dot{u}}_{i} - \dot{u}_h(t)\right) + \underset{\sim}{k}_{a,i}\left(\underset{\sim}{u}_{i}(t) - u_h(t)\right) = -\mu_a \underset{\sim}{m}_{a,i}\underset{\sim}{A}_{cc} e^{j\omega t} \\ \frac{v(t)}{R_l} + C_p\dot{v}(t) = \Theta\dot{u}_h(t) \end{cases} \tag{37}$$

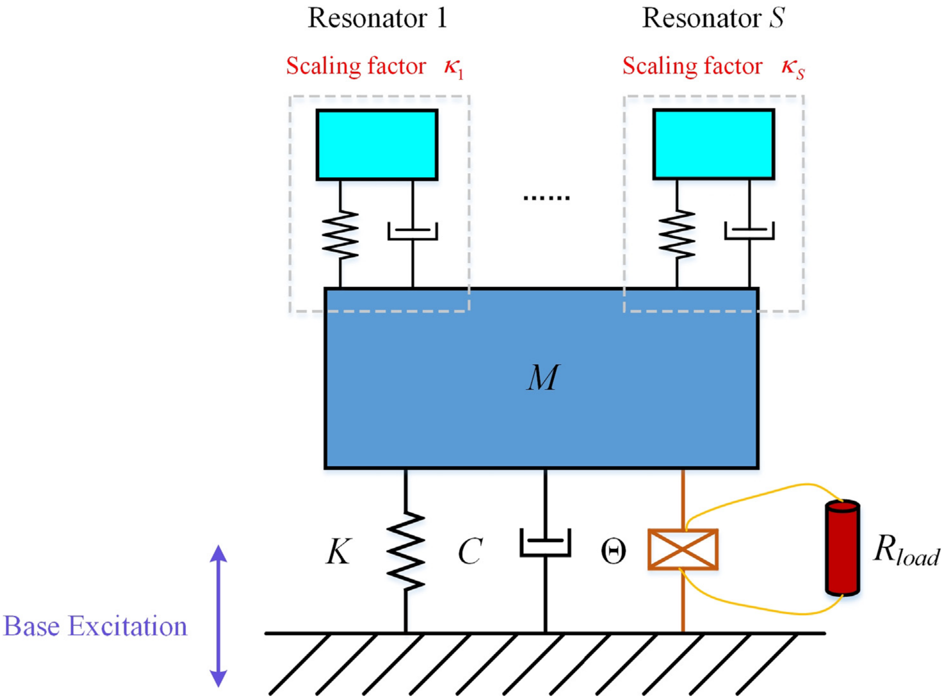

Fig. 5. Equivalent MDOF model of the CombBeam-based PEH under base excitation.

It should be mentioned that apart from the excitation forces on the right hand side of Eq. (37), the mathematical formulation of the MDOF model on the left hand side of Eq. (38), i.e., the employment of the lumped parameters and the correction and scaling factors (α, κ_i), is the same for both base excitation and aerodynamic force excitation. Therefore, though the main purpose of this study is to present the design and the modelling of a CombBeam-based PEH for galloping energy harvesting, a base excitation case study using finite element method will also be presented later to assist the verification of the developed MDOF model. In addition, a small difference between the two excitation cases lies in that $u_i(t)$ and $u_h(t)$ in the aerodynamic force excitation case are absolute displacements.

3.5. MDOF model under aerodynamic force excitation

When the proposed CombBeam-based PEH undergoes galloping vibration in the direction normal to the wind flow, the aerodynamic force exerted onto the bluff body can be expressed as:

$$F_{galloping} = \frac{1}{2}\rho_a S U^2 \sum_{i=1,2\ldots} a_i \left(\frac{\dot{w}_2(L_2,t) + d_c \dot{w}_2'(L_2,t)}{U}\right)^i \tag{38}$$

where ρ_a is the density of the air, S is the characteristic area normal to the wind flow with the speed of U. a_i $(i = 1, 2\ldots)$ are the empirical coefficients for the polynomial fitting. To distinguish it with the CombBeam-based PEH under the base excitation, we refer this system undergoing galloping vibration as CombBeam-based GPEH. The equivalent MDOF model of the CombBeam-based GPEH is shown in Fig. 6. Since the tip displacement of the host beam $w_2(L_2,t)$ has been redefined as $u_h(t)$ for conciseness, Eq. (40) can be rewritten in the form as:

$$F_{galloping} = \frac{1}{2}\rho_a S U^2 \sum_{i=1,2\ldots} a_i \left[\left(1 + \frac{\phi_{2,1}'(L_2)}{\phi_{2,1}(L_2)} d_c\right)\frac{\dot{u}_h(t)}{U}\right]^i \tag{39}$$

The governing equations of the CombBeam-based GPEH can then be established as:

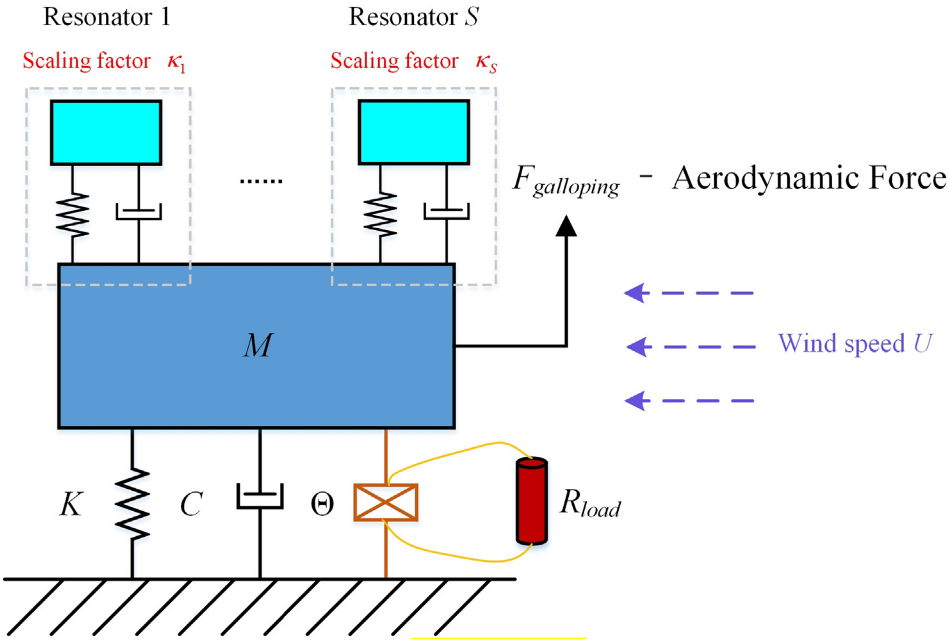

Fig. 6. Equivalent MDOF model of the CombBeam-based GPEH under aerodynamic force excitation.

$$\begin{cases} \left\{ M\ddot{u}_h(t) + D\dot{u}_h(t) + Ku_h(t) + \Theta v(t) + \sum_{i=1}^{S}\alpha\left[\underset{\sim}{c}_{a,i}\left(\dot{u}_h(t) - \dot{\underset{\sim}{u}}_i(t)\right) + \underset{\sim}{k}_{a,i}\left(u_h(t) - \underset{\sim}{u}_i(t)\right)\right]\right\} = F_{galloping} \\ \underset{\sim}{m}_{a,i}\ddot{\underset{\sim}{u}}_i + \underset{\sim}{c}_{a,i}\left(\dot{\underset{\sim}{u}}_i - \dot{u}_h(t)\right) + \underset{\sim}{k}_{a,i}\left(\underset{\sim}{u}_i(t) - u_h(t)\right) = 0 \\ \frac{v(t)}{R_l} + C_p\dot{v}(t) = \Theta\dot{u}_h(t) \end{cases} \tag{40}$$

By introducing the variables:

$$\begin{cases} y_1 = u_h \\ y_2 = \dot{u}_h \\ \quad \cdots \\ y_{2i+1} = \underset{\sim}{u}_i \\ y_{2i+2} = \dot{\underset{\sim}{u}}_i \\ \quad \cdots \\ y_{2S+3} = v(t) \end{cases} \tag{41}$$

Eq. (29) can be rearranged in the state space form as:

$$\begin{cases} \dot{y}_1 = y_2 \\ \dot{y}_2 = \frac{1}{M}\left\{ \begin{array}{l} \frac{1}{2}\rho_a S U^2 \sum_{i=1,2\ldots} a_i\left[\left(1 + \frac{\phi'_{2,1}(L_2)}{\phi_{2,1}(L_2)}d_c\right)\frac{y_2}{U} + \frac{\phi'_{2,1}(L_2)}{\phi_{2,1}(L_2)}y_1\right]^i - Dy_2 - Ky_1 - \Theta y_{2S+3} \\ -\sum_{i=1}^{S}\alpha\left[\underset{\sim}{c}_{a,i}(y_2 - y_{2i+2}) + \underset{\sim}{k}_{a,i}(y_1 - y_{2i+1})\right] \end{array} \right\} \\ \cdots \\ \dot{y}_{2i+1} = y_{2i+2} \\ \dot{y}_{2i+2} = -\frac{1}{\underset{\sim}{m}_{a,i}}\left[\underset{\sim}{c}_{a,i}(y_{2i+2} - y_2) + \underset{\sim}{k}_{a,i}(y_{2i+1} - y_1)\right] \\ \cdots \\ y_{2S+3} = \frac{1}{C_p}\left(\Theta y_2 - \frac{y_{2S+3}}{R_l}\right) \end{cases} \tag{42}$$

which can be solved using a numerical method such as the Runge-Kutta method. It can be found that the analysis based on the developed MDOF model is pretty simple. Though there exist other rigorous modelling methods, the developed MDOF model provides a fast and convenient means for evaluating this kind of system. Moreover, another benefit of the MDOF model is that when it is shunted to complicated interface circuits such as SCE [55], P-SSHI [56], S-SSHI [57] etc., we can easily bridge the structural modelling and the electrical simulation using the formulated simple MDOF model to perform a comprehensive study.

It should be stated that the developed MDOF model is valid for predicting the dynamic behaviour of the proposed system around only the fundamental resonance. As the limit-cycle oscillation of a galloping energy harvester is just around the fundamental natural frequency, the developed MDOF model is sufficient to capture the dynamic characteristics of the proposed system when being used for galloping energy harvesting. On other hand, a resonant-type vibration energy harvester generally delivers the maximum power output around the fundamental resonance. When the proposed system is employed for harvesting energy from base excitation, its power output around the fundamental resonance is most important. In this scenario, the developed MDOF model can work properly to predict the energy harvesting performance.

4. Finite element verification

It can be noted in Sections 3.4 and 3.5 that the MDOF models under the base excitation and the aerodynamic force excitation have exactly the same mathematical formulations except for the forcing terms. This section aims to provide a verification of the developed MDOF model of the CombBeam-based PEH under a base excitation using the commercial finite element software ANSYS.

4.1. Conventional beam PEH

Firstly, a finite element model of the conventional beam PEH as shown in Fig. 7 is built to verify the equivalent lumped parameters derived in Section 3.2. The three-dimensional (3D) 20-node structural solid element SOLID186 is used for the host beam and the tip mass (bluff body). The 3D 20-node coupled-field solid element SOLID226 is used for the piezoelectric transducer. To maintain uniform electrical potentials over the electrodes, the voltage degrees of freedom (DOFs) on the top and bottom surfaces of the piezoelectric transducer are coupled, separately. Then, the two electrodes are coupled to the two nodes of a circuit element CIRCU94 that is defined with a resistance characteristic to emulate the connection to a resistor. In the following case study, we directly use the geometric and material parameters of the fabricated physical prototype presented in Section 5.

The time harmonic base excitation is controlled at an acceleration amplitude of 1 m/s^2. For the given system parameters listed in Table 1, by using Eq. (38), the equivalent lumped parameters of the conventional beam PEH can be derived as: $M = 5.4$ g, $K = 21.963$ N/m, $D = 0.0041$ N·s/m, $\Theta = 3.9657 \times 10^{-5}$N/V and $\mu = 0.4408$. Fig. 8 shows the open-circuit voltage responses of the conventional beam PEH. It should be mentioned that the fundamental natural frequencies of the cantilever beam PEH predicted by the developed SDOF model and the FE model are slightly different, respectively, 11.609 Hz and 11.573 Hz. The relative error of the developed SDOF model is only about 0.31%. To focus on the comparison of the voltage amplitude, the frequency axes for the SDOF model and FE model are normalized by each natural frequency. From Fig. 8(a), it can be seen that the results from both models are in a good agreement. The maximum voltage amplitude calculated by the FE model is 19.53 V. The result predicted by the SDOF model is 19.78 V, which indicates an error of about 1.28%. It is worth mentioning that the SDOF model only considers the fundamental mode of the conventional PEH which is the main cause of the error. To demonstrate this, Fig. 8(b) shows the zoomed-in view of the Fig. 8(a) around the resonance and the analytical result by including the first three modes of the conventional beam PEH is also provided. It can be found that the maximum

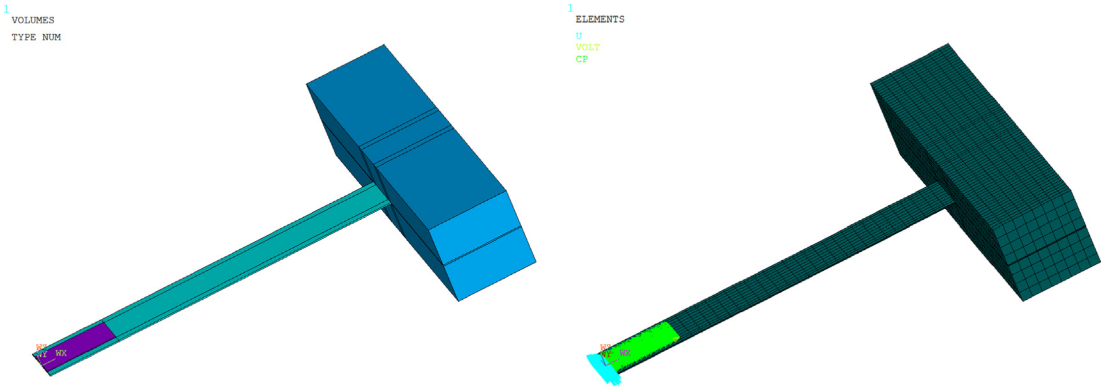

(a) (b)

Fig. 7. (a) The geometric and (b) mesh models of the conventional beam PEH.

Table 1
Geometric and material parameters of the conventional beam PEH.

Beam			
Length	140 mm	Material density	2700 kg/m^3
Width	20 mm	Young's modulus	70 GPa
Thickness	0.5 mm	Poisson's ratio	0.3
Tip Mass (Bluff Body)			
Length	140 mm	Material density	16 kg/m^3
Width	32 mm	Young's modulus	700 MPa
Thickness	32 mm	Poisson's ratio	0.3
Piezoelectric Transducer			
Length	28 mm	Material density	5440 kg/m^3
Width	14 mm	Young's modulus	30.336 GPa
Thickness	0.3 mm	Poisson's ratio	0.3
Piezoelectric constant d_{31}	−120 pC/N	permittivityε_{33}^S	2.3556 × 10^{-8}F/m

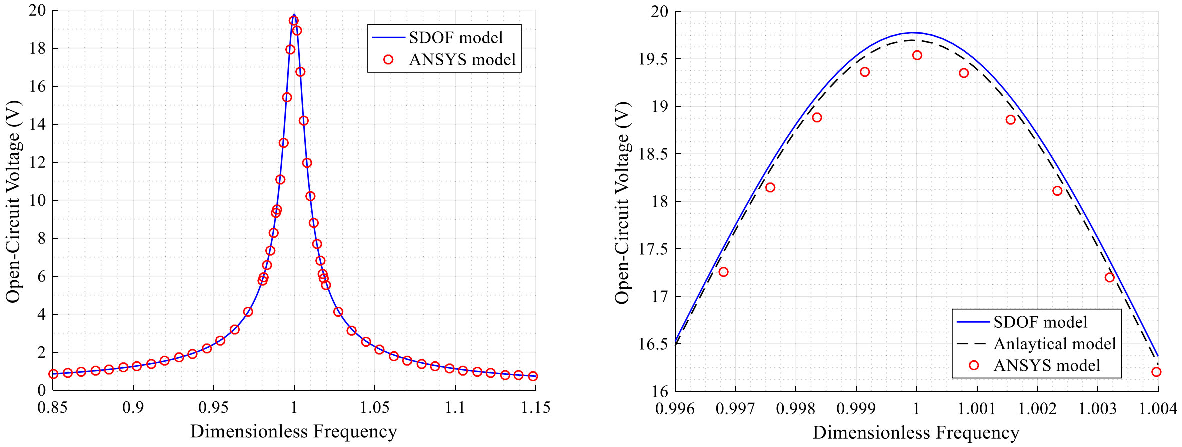

(a) (b)

Fig. 8. (a) Open-circuit voltage response of the conventional beam PEH and (b) the zoomed-in view around the resonance.

voltage amplitude from the analytical model is about 19.7 V and the relative error is reduced to 0.87%. However, since the relative error of the SDOF model is minor, the SDOF model can be regarded as being successfully verified, thus the derived equivalent lumped parameters. This means that for the conventional beam PEH, around its fundamental resonance, using the fundamental mode is sufficiently accurate to describe its dynamic behaviour and it is therefore regarded as a SDOF system around the fundamental resonance and we often refer it as a SDOF PEH.

4.2. Reaction force of SDOF model of parasitic beam

Though the SDOF model of a pure cantilever beam has been validated and widely used in the literature, the reaction force correction factor α presented in Section 3.1 is proposed for the first time. Hence, before proceeding to the verification of the MDOF model of the CombBeam-based PEH, we perform a verification of the derived reaction force correction factor α through the comparison with a corresponding finite element model. The geometric and material parameters of the parasitic beam of the fabricated physical prototype that will be introduced in Section 5 is directly used in the following verification study. The mass density and the Young's modulus of the parasitic beam are 7800 kg/m^3 and 200 GPa, respectively. The length, width and thickness are 40 mm, 8 mm and 0.1 mm, respectively. For the controlled base excitation of 1 m/s^2, Fig. 9 shows the frequency response of the reaction force at the root of the cantilever beam. The blue solid line and the black dashed line denote the result of the SDOF models using and not using the derived correction factor α, respectively. The red circle denotes the result from ANSYS. The results in Fig. 9(a) and (b) correspond to the configuration with a tip mass of 0 g and 5 g, respectively. It can be observed that when the tip mass is 0 g (Fig. 9(a)), the traditional SDOF model without using α produces a remarkable error in predicting the reaction force. Correcting the reaction force using the derived α significantly improves the accuracy and reduces the relative error from 35.74% to 0.626%. When the tip mass is increased to 5 g (Fig. 9(b)), all the three curves almost coincide with each other, which means that omitting the correction factor α does not make any noticeable influence given a relatively heavy tip mass.

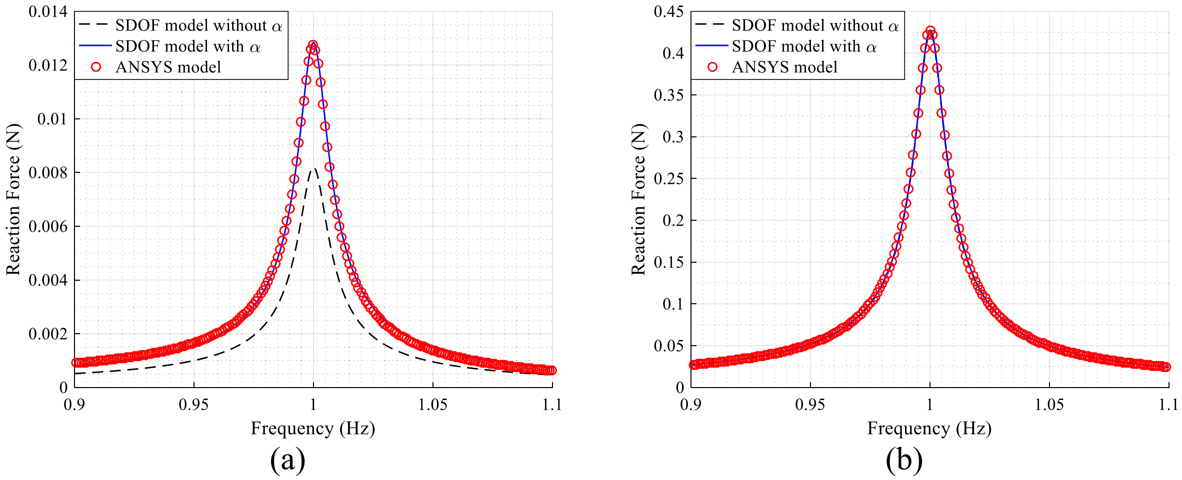

Fig. 9. Reaction force frequency response when the tip mass is (a) 0 g and (b) 5 g.

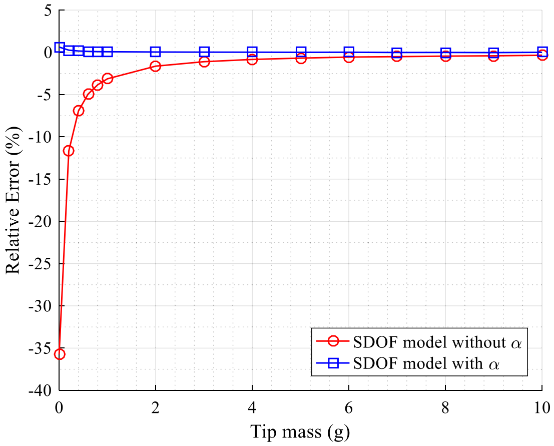

Fig. 10. Relative errors of the SDOF model in predicting the reaction force using and without using the correction factor α for different tip masses.

To give more insights into the importance of the reaction force correction factor α, Fig. 10 shows the relative errors of the SDOF model in predicting the reaction force as a function of the tip mass. It can be found that the prediction error is always very minor and can be neglected when the correction factor α is used. However, if the factor α is not used to conduct the correction, the relative error can be very remarkable: when the tip mas is 0 g, the relative error is about 35.74%. Moreover, we can note that with the increase of the tip mass, the relative error of forgetting to use the correction factor α decreases: when the tip mass is increased to 10 g, the prediction error is reduced to 0.34%. It should be noted that the relative error not only depends on the tip mass, but also varies with the beam stiffness which is dependent on its geometric and material parameters. Therefore, to ensure an accurate prediction of the reaction force, the correction factor α is recommended to be always used.

4.3. CombBeam-based PEH

After having verified the SDOF model of the conventional beam PEH and the reaction force factor α, we now proceed to the verification of the MDOF model for the CombBeam-based PEH whose geometric and mesh models are shown in Fig. 11(a) and (b), respectively. The parasitic beam is also emulated using the 3D 20-node structural solid element SOLID186. The geometric and material parameters of the parasitic beam have already been given in Section 4.2. The host beam and the tip mass are the same as those for the conventional beam PEH as presented in Section 4.1. The mounting positions of the parasitic beams are annotated in Fig. 11(a).

It should be mentioned that for the physical prototype, the tip mass attached to the parasitic beam is 1.8 g. Using the SDOF representation method developed in Section 3.1 and noting that a pair of parasitic beams are represented as a single local resonator, the equivalent lumped parameters of the local resonator can be calculated as: m_a = 3.7 g, k_a = 12.5 N/m, c_a = 0.

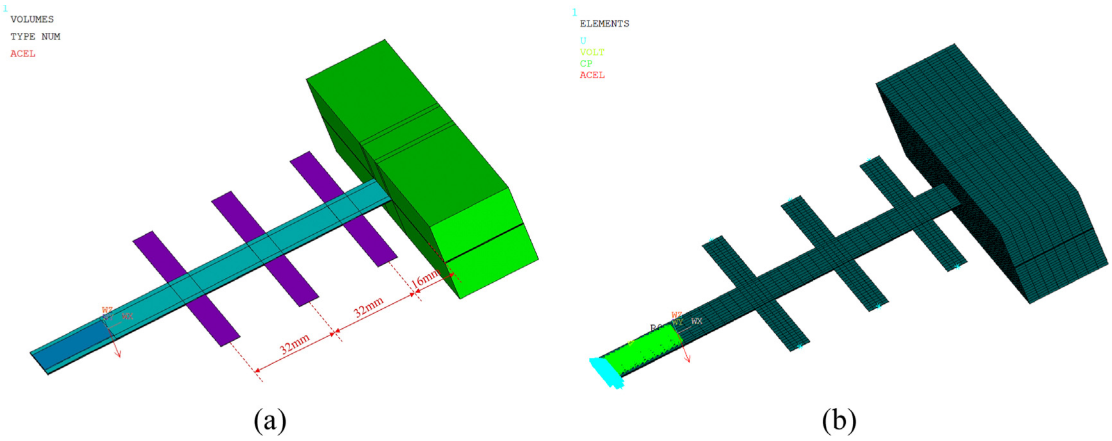

Fig. 11. (a) The geometric and (b) mesh models of the CombBeam-based PEH.

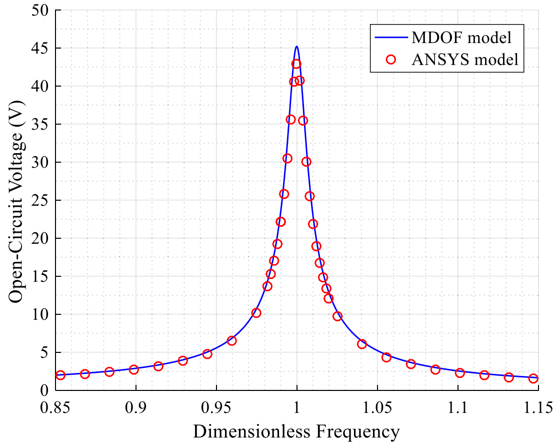

Fig. 12. Open-circuit voltage response of the CombBeam-based PEH.

0026 N·s/m, μ_a = 1.0187 and α = 1.0187. The scaling factors for the three parasitic beams being mounted from the root to the tip of the host beam are κ_1 = 0.1849, κ_2 = 0.4585 and κ_3 = 0.8089, respectively. Under the base excitation of 1 m/s^2, Fig. 12 shows the voltage response of the CombBeam-based PEH that corresponds to the physical prototype. The fundamental natural frequencies of the CombBeam-based PEH predicted by the developed MDOF model and the FE model are 6.876 Hz and 6.573 Hz, respectively. The relative error of the developed MDOF model in predicting the fundamental natural frequency is about 4.60%. The maximum voltage amplitudes calculated using the developed MDOF model and the FE model are 45.21 V and 42.86 V, respectively, which indicates that the developed MDOF model overestimates the maximum voltage amplitude for about 5.48%.

In the modelling of the CombBeam-based PEH, the parasitic beams are converted to equivalent mass-spring systems being attached at a series of discrete points on the host beam. However, in the practical physical prototype, the width of the parasitic beam has a certain dimension. Thus, this leads to the discrepancy between the MDOF model and the FE model. To prove this speculation, Fig. 13 compares the results from the MDOF model and the FE model by varying the width of the parasitic beam. From Fig. 13(a) and (b), we can see that with the decrease of the width of the parasitic beam, the fundamental natural frequencies and the maximum open-circuit voltage amplitudes predicted by both models get closer. Fig. 13(c) shows the corresponding relative errors of Fig. 13(a) and (b) and verifies that with the decrease of the width of the parasitic beam, the prediction error of the MDOF model decreases. Due to the complexity of the structural architecture of the CombBeam-based PEH, the developed MDOF model can be regarded as a convenient means to provide a fast performance evaluation of the proposed CombBeam-based PEH.

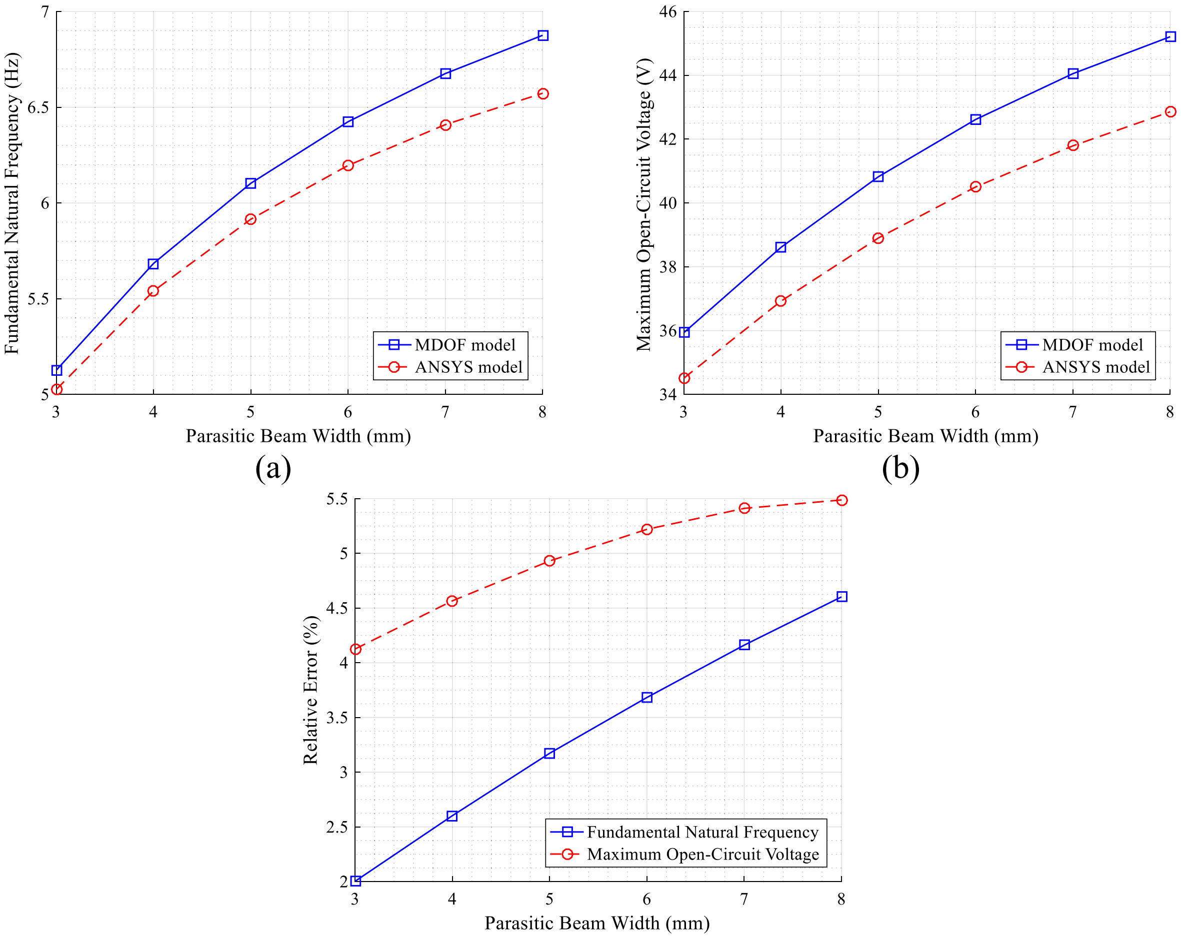

(a) (b) (c)

Fig. 13. (a) Fundamental natural frequency, (b) maximum open-circuit voltage of the CombBeam-based PEH predicted by the MDOF model and the FE model, (c) the relative errors of the MDOF model in terms of predicting the fundamental natural frequency and the maximum open-circuit voltage.

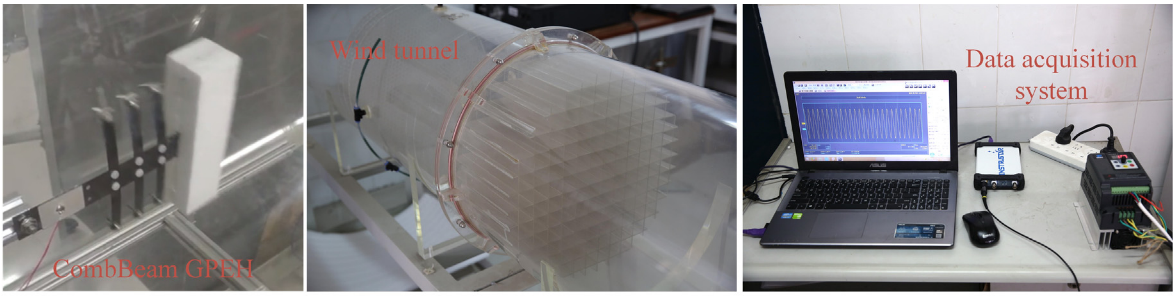

(a) (b) (c)

Fig. 14. (a) Physical prototype of the CombBeam-based GPEH, (b) wind tunnel setup and (c) data acquisition system.

5. Experimental validation and comparative analysis

The results under the base excitation in Section 4 have validated the MDOF model in terms of the derived lumped parameters, scaling factors and correction factors. To further validate the developed MDOF model under aerodynamic force excitation as presented in Section 3.5, an experimental study is performed. Fig. 14(a), (b) and (c) show the fabricated physical prototype, the wind tunnel setup and the data acquisition system, respectively. The detailed system parameters of the fabricated physical prototype have been given in the previous sections. The tunnel for producing the incident air flow has a round cross-section with a diameter of 400 mm. A hot-wire anemometer is used to measure the wind speed. The system damping ratios are measured based on a free vibration decay test. The damping ratios of the host beam along with the bluff body and the parasitic beam for their first modes are 0.0267 and 0.007, respectively. In the theoretical calculation, we assume that the damping ratios are constant in the low frequency regime below their fundamental natural frequencies. The characteristic dimension of the cross-section of the wind tunnel is 0.4 m, the operation wind speed in the following case study is beyond 1.5 m/s, the kinematic viscosity is 1.5×10^{-5} at the temperature of 20°, the corresponding Reynolds number is larger than 40000. Therefore, the empirical aerodynamic coefficients presented in Eq. can be referred to [17]: a_1 = 2.3, a_2 = 0 and a_3 = -18, which were experimentally determined for a square-sectioned bluff body under the laminar flow with a high Reynolds number larger than 33000.

The experimentally measured and the SDOF/MDOF model predicted open-circuit voltage amplitudes versus the wind speed are presented in Fig. 15. The black square and the red line affixed with asterisk marks denote the experimentally measured and the SDOF model predicted open-circuit voltage amplitudes of the conventional beam GPEH, respectively. The blue circle and the pink line affixed with plus marks denote the experimentally measured and the MDOF model predicted results of the CombBeam-based GPEH, respectively. The cut-in wind speeds of the conventional beam GPEH measured from the experiment and predicted by the SDOF model are 2.24 m/s and 2.3 m/s, respectively. The cut-in wind speeds of the CombBeam-based GPEH measured from the experiment and predicted by the MDOF model are 1.96 m/s and 2.0 m/s, respectively. The error and discrepancy may partly come from the inaccuracy of the MDOF model that has been discussed in Section 4.3. In general, the developed SDOF and MDOF models give good predictions in terms of the cut-in wind speeds of the conventional and CombBeam-based GPEHs. From both the experimental result and the numerical result calculated by the SDOF/MDOF model, the cut-in wind speed of the CombBeam-based GPEH is reduced as compared to the conventional beam GPEH, which indicates that the CombBeam-based GPEH has an advantage over the conventional beam GPEH for low-speed wind energy harvesting. Moreover, it can be observed from both the experimental and numerical results, the open-circuit voltage amplitude increases monotonically with the increase of the wind speed for both the conventional beam and CombBeam-based GPEHs. In addition, the voltage amplitude of the CombBeam-based GPEH is always larger than that of the conventional beam GPEH under any wind speed. Hence, the CombBeam-based GPEH demonstrates a better energy harvesting performance than the conventional beam GPEH.

With the validated model of CombBeam-based GPEH, under the wind speed of 3 m/s, Fig. 16 further shows the simulated transient open-circuit voltage responses of the conventional beam and CombBeam-based GPEHs. As shown in Fig. 16(a) and (c), under the aerodynamic force, the conventional beam/CombBeam-based GPEH starts to vibrate until a steady-state limit-cycle is reached as shown in Fig. 16(b) and (d). At the wind speed of 3 m/s, the CombBeam-based GPEH produces a voltage output amplitude of 20.57 V which is much larger than that of the conventional beam GPEH (i.e., 10.02 V). Besides that, from the steady-state responses presented in Fig. 16(b) and (d), we can note that the oscillation frequency of the CombBeam-based GPEH is reduced as compared to the conventional beam GPEH. The limit cycle oscillation occurs very close to the resonant frequency of the system. The fundamental natural frequencies of the conventional beam and CombBeam-based GPEHs have been calculated and presented in Section 4. The phenomenon observed in terms of frequencies in Fig. 16.(b) and (d) is in agreement with the calculated results in Section 4.

Fig. 17 further shows the power responses of the conventional beam and CombBeam-based GPEHs for different wind speeds and load resistances. Though the existing theory indicates that the cut-in wind speed depends on the system damping that constitutes the mechanical and electrical damping components and varies with the change of the load resistance

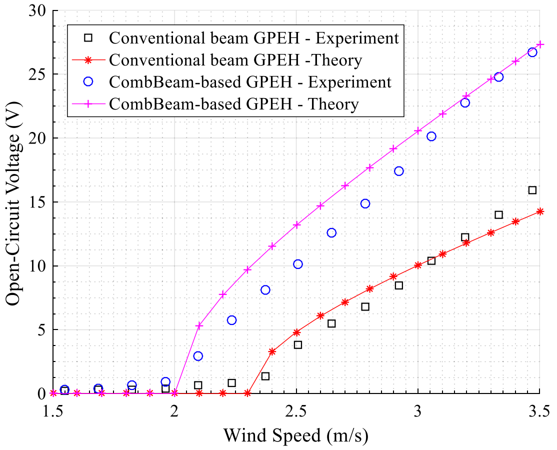

Fig. 15. Experimentally measured and SDOF/MDOF model predicted open-circuit voltage amplitudes of conventional beam and CombBeam-based GPEHs versus wind speed.

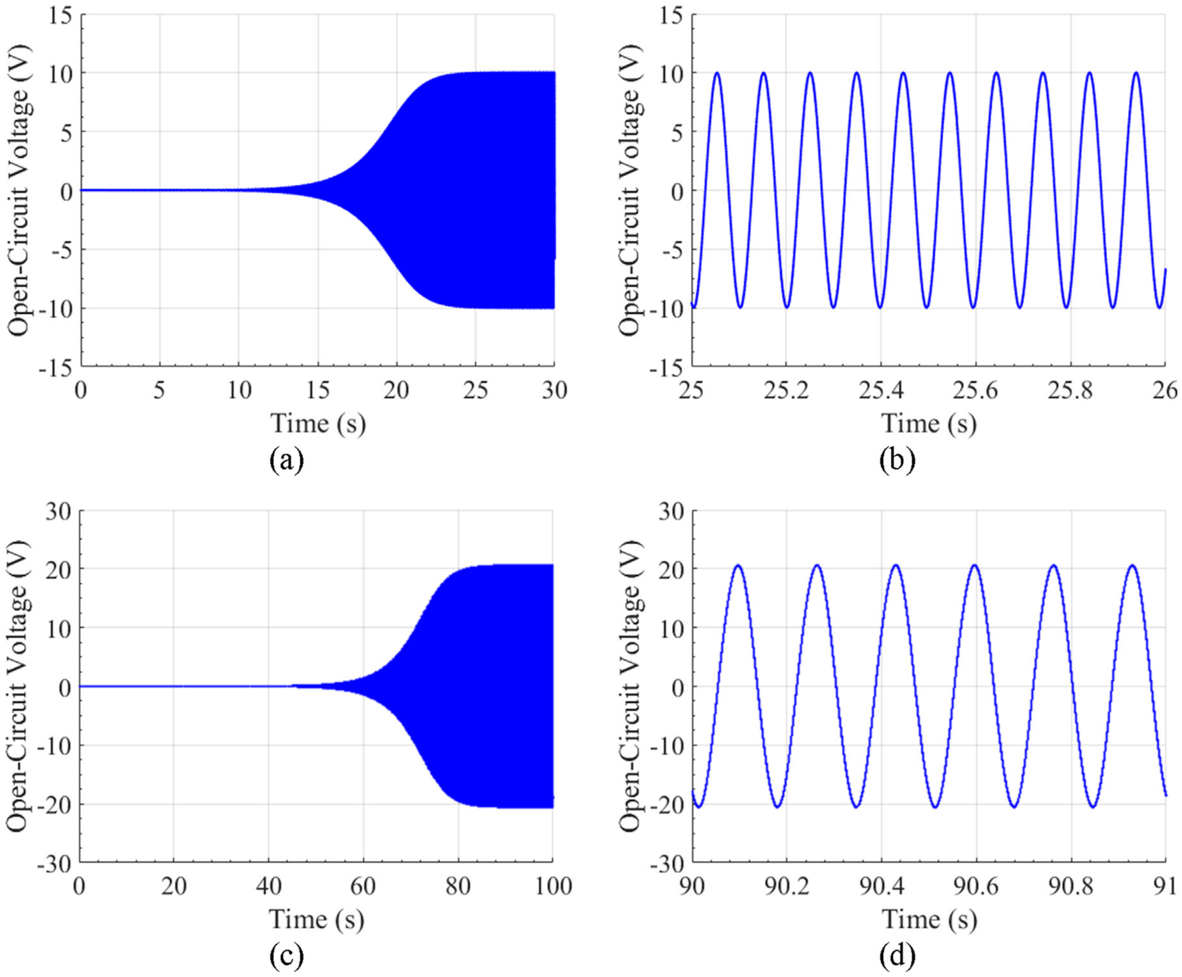

Fig. 16. Transient open-circuit voltage responses of the conventional beam and CombBeam-based GPEHs under the wind speed of 3 m/s from numerical simulation: (a) time history of the open-circuit voltage of the conventional beam GPEH, and (b) its zoomed-in view in steady-state; (c) time history of the open-circuit voltage of the CombBeam-based GPEH, and (d) its zoomed-in view in steady-state.

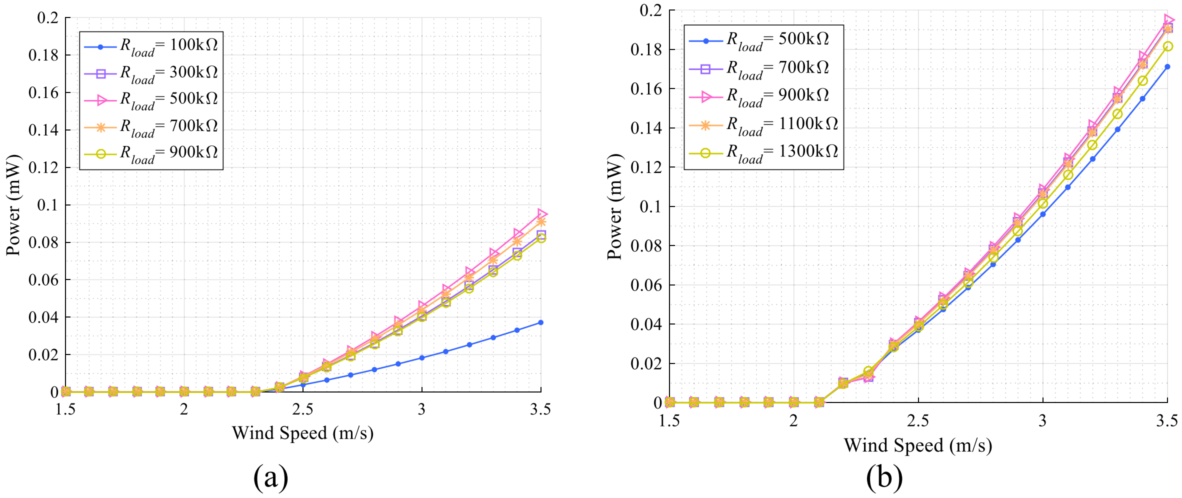

Fig. 17. Power response versus wind speed for different load resistances: (a) conventional beam GPEH, (b) CombBeam-based GPEH.

[37], from Fig. 17, we find that the cut-in wind speeds of both the conventional beam and CombBeam-based GPEHs are insensitive to the change of the load resistance. This is because the electromechanical coupling of both systems are very weak. Though the electrical damping varies with the change of the load resistance, the overall system damping has no obvious change. To support the above explanation, we can use the criterion presented in [58] to prove that both GPEHs studied in this work are weak coupling systems. We define $k_e^2 = \Theta^2/C_pK$ as a non-dimensionless coupling coefficient. $k_c^2 = 4\zeta + 4\zeta^2$ is a critical value that can be used to judge whether a PEH is a strong or weak coupling system [58]. $k_e^2 < k_c^2$ indicates that the PEH is a weak coupling system. Otherwise, it is a strong coupling system. For the conventional beam GPEH, the non-dimensionless coupling coefficient can be calculated as $k_e^2 = 0.0023$ using the derived lumped parameters in Section 4.1. The critical value is calculated as $k_c^2 = 0.1097$ using the experimentally determined damping ratio of $\zeta = 0.0267$. Since $k_e^2 = 0.0023 \; < < k_c^2 = 0.1097$, it is proved that the conventional beam GPEH studied in this work is a weak coupling system. Though the above criterion only applies for a SDOF system, we can speculate that the CombBeam-based GPEH must also be a weak coupling system, as the introduced parasitic beams are pure mechanical structures and cannot increase the coupling coefficient of the CombBeam-based GPEH.

Regarding the output power amplitude, for the conventional beam GPEH, it is noted in Fig. 17(a) that the power output increases with R_{load} up to 500kΩ then decreases when R_{load} further increases. The optimal power is obtained around 500kΩ. It is revealed in Fig. 17(b) that the optimal resistance for the CombBeam-based beam GPEH is around 900kΩ. As compared to the conventional beam GPEH, the power output from the CombBeam-based GPEH is substantially increased. For instance, under the same wind speed of 3 m/s, the optimal power of the CombBeam-based GPEH is about 0.1245mW, while the optimal power of the conventional beam GPEH is only about 0.0459mW. Therefore, it can be seen that the CombBeam-based GPEH exhibits a significantly enhanced energy harvesting performance.

6. Conclusions

This paper has developed a CombBeam-based galloping energy harvesting system. A MDOF model has been established for such a system by simplifying the host beam and parasitic beams as SDOF systems and deriving equivalent lumped parameters, various correction factors and scaling factors. The MDOF model was first successfully verified by finite element method in the base excitation case. A prototype of the CombBeam-based GPEH was then built and the wind tunnel test further validated the MDOF model in the aerodynamic excitation scenario. The result shows that the fundamental natural frequency of the CombBeam-based GPEH is decreased and the cut-in wind speed is reduced for about 12.5% as compared to a conventional beam GPEH, which indicates the advantage of the CombBeam-based GPEH for low-speed wind energy harvesting. From the energy harvesting perspective, it is found that both the open-circuit voltage and the power output around the optimal load resistance are increased by using the CombBeam-based GPEH. For a specific instance, under the same wind speed of 3 m/s, the optimal power output of the CombBeam-based GPEH is increased by about 171.2% as compared to the conventional beam GPEH.

Declaration of Competing Interest

The authors declare that they have no known competing financial interests or personal relationships that could have appeared to influence the work reported in this paper.

Acknowledgement

This work was supported by National Natural Science Foundation of China (Grant No. 51977196), China Postdoctoral Science Foundation (Grant No. 2020T130557), and the Key Projects of Higher Education in Henan Province (Grant No. 18A470016).

References

[1] J. Wang, L. Geng, L. Ding, H. Zhu, D. Yurchenko, The state-of-the-art review on energy harvesting from flow-induced vibrations, Appl. Energy 267 (2020) 114902.
[2] J. Wang, G. Hu, Z. Su, G. Li, W. Zhao, L. Tang, L. Zhao, A cross-coupled dual-beam for multi-directional energy harvesting from vortex induced vibrations, Smart Mater. Struct. 28 (12) (2019) 12LT02.
[3] G. Hu, L. Tang, R. Das, P. Marzocca, A two-degree-of-freedom piezoelectric energy harvester with stoppers for achieving enhanced performance, Int. J. Mech. Sci. 149 (2018) 500–507.
[4] S. Fang, X. Fu, X. Du, W.-H. Liao, A music-box-like extended rotational plucking energy harvester with multiple piezoelectric cantilevers, Appl. Phys. Lett. 114 (23) (2019) 233902.
[5] A. Erturk, D.J. Inman, A distributed parameter electromechanical model for cantilevered piezoelectric energy harvesters, J. Vibrat. Acoust. Trans. ASME 130 (4) (2008) 041002.
[6] C. Lan, L. Tang, R.L. Harne, Comparative methods to assess harmonic response of nonlinear piezoelectric energy harvesters interfaced with AC and DC circuits, J. Sound Vib. 421 (2018) 61–78.
[7] K. Yang, S. Kewei, J. Wang, J. Wang, K. Yin, G. Litak, Piezoelectric wind energy harvesting subjected to the conjunction of vortex-induced vibration and galloping: comprehensive parametric study and optimization, Smart Mater. Struct. (2020).

[8] J. Wang, L. Tang, L. Zhao, Z. Zhang, Efficiency investigation on energy harvesting from airflows in HVAC system based on galloping of isosceles triangle sectioned bluff bodies, Energy 172 (2019) 1066–1078.

[9] W. Liu, A. Badel, F. Formosa, Y. Wu, A. Agbossou, Novel piezoelectric bistable oscillator architecture for wideband vibration energy harvesting, Smart Mater. Struct. 22 (3) (2013) 035013.

[10] A. Erturk, D.J. Inman, On mechanical modeling of cantilevered piezoelectric vibration energy harvesters, J. Intell. Mater. Syst. Struct. 19 (11) (2008) 1311–1325.

[11] A. Erturk, D.J. Inman, Issues in mathematical modeling of piezoelectric energy harvesters, Smart Mater. Struct. 17 (6) (2008) 065016.

[12] L. Tang, Y. Yang, A nonlinear piezoelectric energy harvester with magnetic oscillator, Appl. Phys. Lett. 101 (9) (2012) 094102.

[13] H. Zhu, G. Li, J. Wang, Flow-induced vibration of a circular cylinder with splitter plates placed upstream and downstream individually and simultaneously, Appl. Ocean Res. 97 (2020) 102084.

[14] Q. Zou, L. Ding, H. Wang, J. Wang, L. Zhang, Two-degree-of-freedom flow-induced vibration of a rotating circular cylinder, Ocean Eng. 191 (2019) 106505.

[15] Y. Yang, L. Zhao, L. Tang, Comparative study of tip cross-sections for efficient galloping energy harvesting, Appl. Phys. Lett. 102 (6) (2013) 064105.

[16] Ali, M., M. Arafa, and M. Elaraby. Harvesting energy from galloping oscillations. in Proceedings of the world Congress on Engineering. 2013. WCE.

[17] A. Barrero-Gil, G. Alonso, A. Sanz-Andres, Energy harvesting from transverse galloping, J. Sound Vib. 329 (14) (2010) 2873–2883.

[18] M. Zhang, G. Hu, J. Wang, Bluff body with built-in piezoelectric cantilever for flow-induced energy harvesting, Int. J. Energy Res. 44 (5) (2020) 3762–3777.

[19] A. Bibo, A.H. Alhadidi, M.F. Daqaq, Exploiting a nonlinear restoring force to improve the performance of flow energy harvesters, J. Appl. Phys. 117 (4) (2015) 045103.

[20] G. Hu, J. Wang, Z. Su, G. Li, H. Peng, K. Kwok, Performance evaluation of twin piezoelectric wind energy harvesters under mutual interference, Appl. Phys. Lett. 115 (7) (2019) 073901.

[21] J. Wang, L. Geng, K. Yang, L. Zhao, F. Wang, D. Yurchenko, Dynamics of the double-beam piezo-magneto-elastic nonlinear wind energy harvester exhibiting galloping-based vibration, Nonlinear Dyn. (2020).

[22] H. Akaydın, N. Elvin, Y. Andreopoulos, Wake of a cylinder: a paradigm for energy harvesting with piezoelectric materials, Exp. Fluids 49 (1) (2010) 291–304.

[23] Z. Yan, L. Wang, M.R. Hajj, Z. Yan, Y. Sun, T. Tan, Energy harvesting from iced-conductor inspired wake galloping, Extreme Mech. Lett. (2020) 100633.

[24] Z. Zhou, W. Qin, P. Zhu, W. Du, W. Deng, J. Pan, Scavenging wind energy by a dynamic-stable flutter energy harvester with rectangular wing, Appl. Phys. Lett. 114 (24) (2019) 243902.

[25] J. Wang, L. Tang, L. Zhao, G. Hu, R. Song, K. Xu, Equivalent circuit representation of a vortex-induced vibration-based energy harvester using a semi-empirical lumped parameter approach, Int. J. Energy Res. 44 (6) (2020) 4516–4528.

[26] J. Wang, S. Gu, C. Zhang, G. Hu, G. Chen, K. Yang, H. Li, G. Litak, D. Yurchenko, Hybrid wind energy scavenging by coupling vortex-induced vibrations and galloping, Energy Convers. Manage. 213 (2020) 112835.

[27] A. Barrero-Gil, S. Pindado, S. Avila, Extracting energy from vortex-induced vibrations: a parametric study, Appl. Math. Model. 36 (7) (2012) 3153–3160.

[28] S. Zhou, J. Wang, Dual serial vortex-induced energy harvesting system for enhanced energy harvesting, AIP Adv. 8 (7) (2018) 075221.

[29] E. Arroyo, A. Badel, F. Formosa, Y. Wu, J. Qiu, Comparison of electromagnetic and piezoelectric vibration energy harvesters: Model and experiments, Sens. Actuat. A 183 (2012) 148–156.

[30] Y. Zhang, T. Wang, A. Luo, Y. Hu, X. Li, F. Wang, Micro electrostatic energy harvester with both broad bandwidth and high normalized power density, Appl. Energy 212 (2018) 362–371.

[31] IEEE Standard on piezoelectricity. Ieee Transactions on Ultrasonics Ferroelectrics and Frequency Control, 1996. 43(5): p. A1-A54.

[32] S. Priya, Advances in energy harvesting using low profile piezoelectric transducers, J. Electroceram. 19 (1) (2007) 167–184.

[33] J. Sirohi, R. Mahadik, Harvesting wind energy using a galloping piezoelectric beam, J. Vib. Acoust. 134 (1) (2012) 011009.

[34] Erturk, A. and D.J. Inman. Mechanical considerations for modeling of vibration-based energy harvesters. in Proceedings of the ASME IDETC 21st Biennial Conference on Mechanical Vibration and Noise. 2007.

[35] Hu, G., B. Zhao, L. Tang, J. Liang, and R. Das. Modeling of partially covered piezoelectric energy harvester connected to SEH interface circuit. 2018. KATHOLIEKE UNIV LEUVEN, DEPT WERKTUIGKUNDE.

[36] L. Zhao, Y. Yang, Analytical solutions for galloping-based piezoelectric energy harvesters with various interfacing circuits, Smart Mater. Struct. 24 (7) (2015) 075023.

[37] L. Tang, L. Zhao, Y. Yang, E. Lefeuvre, Equivalent circuit representation and analysis of galloping-based wind energy harvesting, IEEE/ASME Trans. Mechatron. 20 (2) (2014) 834–844.

[38] K. Yang, J. Wang, D. Yurchenko, A double-beam piezo-magneto-elastic wind energy harvester for improving the galloping-based energy harvesting, Appl. Phys. Lett. 115 (19) (2019) 193901.

[39] J. Wang, S. Zhou, Z. Zhang, D. Yurchenko, High-performance piezoelectric wind energy harvester with Y-shaped attachments, Energy Convers. Manage. 181 (2019) 645–652.

[40] L. Zhao, L. Tang, Y. Yang, Enhanced piezoelectric galloping energy harvesting using 2 degree-of-freedom cut-out cantilever with magnetic interaction, Jpn. J. Appl. Phys. 53 (6) (2014) 060302.

[41] Z.Y. Liu, X.X. Zhang, Y.W. Mao, Y.Y. Zhu, Z.Y. Yang, C.T. Chan, P. Sheng, Locally resonant sonic materials, Science 289 (5485) (2000) 1734–1736.

[42] N. Fang, D. Xi, J. Xu, M. Ambati, W. Srituravanich, C. Sun, X. Zhang, Ultrasonic metamaterials with negative modulus, Nat Mater 5 (6) (2006) 452–456.

[43] G. Hu, L. Tang, J. Xu, C. Lan, R. Das, Metamaterial with local resonators coupled by negative stiffness springs for enhanced vibration suppression, J. Appl. Mech. 86 (8) (2019) 081009.

[44] M. Carrara, M.R. Cacan, J. Toussaint, M.J. Leamy, M. Ruzzene, A. Erturk, Metamaterial-inspired structures and concepts for elastoacoustic wave energy harvesting, Smart Mater. Struct. 22 (6) (2013) 065004.

[45] Z. Chen, Y. Yang, Z. Lu, Y. Luo, Broadband characteristics of vibration energy harvesting using one-dimensional phononic piezoelectric cantilever beams, Phys. B 410 (2013) 5–12.

[46] K. Mikoshiba, J.M. Manimala, C. Sun, Energy harvesting using an array of multifunctional resonators, J. Intell. Mater. Syst. Struct. 24 (2) (2013) 168–179.

[47] G. Hu, L. Tang, A. Banerjee, R. Das, Metastructure with piezoelectric element for simultaneous vibration suppression and energy harvesting, J. Vib. Acoust. 139 (1) (2017) 011012.

[48] G. Hu, L. Tang, R. Das, General framework for modeling multifunctional metamaterial beam based on a derived one-dimensional piezoelectric composite finite element, J. Aerosp. Eng. 31 (6) (2018) 04018088.

[49] G. Hu, L. Tang, R. Das, Internally coupled metamaterial beam for simultaneous vibration suppression and low frequency energy harvesting, J. Appl. Phys. 123 (5) (2018) 055107.

[50] C. Sugino, A. Erturk, Analysis of multifunctional piezoelectric metastructures for low-frequency bandgap formation and energy harvesting, J. Phys. D Appl. Phys. 51 (21) (2018) 215103.

[51] L. Shen, J. Wu, S. Zhang, Z. Liu, J. Li, Low-frequency vibration energy harvesting using a locally resonant phononic crystal plate with spiral beams, Mod. Phys. Lett. B 29 (1) (2015) 1450259.

[52] G.-S. Liu, Y.-Y. Peng, M.-H. Liu, X.-Y. Zou, J.-C. Cheng, Broadband acoustic energy harvesting metasurface with coupled Helmholtz resonators, Appl. Phys. Lett. 113 (15) (2018) 153503.

[53] Z. Chen, Y. Xia, J. He, Y. Xiong, G. Wang, Elastic-electro-mechanical modeling and analysis of piezoelectric metamaterial plate with a self-powered synchronized charge extraction circuit for vibration energy harvesting, Mech. Syst. Sig. Process. 143 (2020) 106824.

[54] G. Hu, L. Tang, J. Liang, R. Das, Modelling of a cantilevered energy harvester with partial piezoelectric coverage and shunted to practical interface circuits, J. Intell. Mater. Syst. Struct. 30 (13) (2019), 1045389X19849269.

[55] Y.P. Wu, A. Badel, F. Formosa, W.Q. Liu, A.E. Agbossou, Piezoelectric vibration energy harvesting by optimized synchronous electric charge extraction, J. Intell. Mater. Syst. Struct. 24 (12) (2013) 1445–1458.

[56] W. Liu, Y. Huang, J. Wang, G. Qin, Energy current analysis of an improved self-adaptive mechatronic approach for P-SSHI, IEEE Trans. Ind. Electron. (2020).

[57] J. Liang, W. Liao, On the influence of transducer internal loss in piezoelectric energy harvesting with SSHI interface, J. Intell. Mater. Syst. Struct. 22 (5) (2011) 503–512.

[58] Y. Liao, H. Sodano, Optimal power, power limit and damping of vibration based piezoelectric power harvesters, Smart Mater. Struct. 27 (7) (2018) 075057.